



## Fabricating high temperature stable Mo-Co<sub>9</sub>S<sub>8</sub>/Al<sub>2</sub>O<sub>3</sub> catalyst for selective hydrodeoxygenation of lignin to arenes

Xinyong Diao<sup>a,1</sup>, Na Ji<sup>a,\*1</sup>, Xinxin Li<sup>a,b</sup>, Yue Rong<sup>a</sup>, Yujun Zhao<sup>c</sup>, Xuebin Lu<sup>a</sup>, Chunfeng Song<sup>a</sup>, Caixia Liu<sup>a</sup>, Guanyi Chen<sup>d</sup>, Longlong Ma<sup>e</sup>, Shurong Wang<sup>f</sup>, Qingling Liu<sup>a,\*</sup>, Changzhi Li<sup>b,\*</sup>

<sup>a</sup> School of Environmental Science and Engineering, Tianjin Key Laboratory of Biomass/Wastes Utilization, Tianjin University, 300350 Tianjin, China

<sup>b</sup> CAS Key Laboratory of Science and Technology on Applied Catalysis, Dalian Institute of Chemical Physics, Chinese Academy of Sciences, Dalian 116023, China

<sup>c</sup> School of Chemical Engineering, Tianjin University, 300350 Tianjin, China

<sup>d</sup> Tianjin University of Commerce, 300134 Tianjin, China

<sup>e</sup> Guangdong Provincial Key Laboratory of New and Renewable Energy Research and Development, Guangzhou Institute of Energy Conversion, Chinese Academy of Sciences, Guangzhou 510640, China

<sup>f</sup> State Key Laboratory of Clean Energy Utilization, Zhejiang University, Hangzhou 310027, China

### ARTICLE INFO

#### Keywords:

Sulfide catalyst

Stability

Lignin

Hydrodeoxygenation

Mo-Co<sub>9</sub>S<sub>8</sub> structure

Arenes

### ABSTRACT

Achieving high-temperature stability/duration without compromising the activity remains an arduous task in catalyst design, particularly for MoS<sub>2</sub> materials. Herein, a robust catalyst with Mo doped Co<sub>9</sub>S<sub>8</sub> nanoparticles anchored on Al<sub>2</sub>O<sub>3</sub> matrix is fabricated, which could selectively convert lignin to arenes with high hydrodeoxygenation activity, selectivity and particularly excellent stability. In the hydrodeoxygenation of diphenyl ether, this catalyst afforded 99.8% conversion and 91.0% yield of benzene at 265 °C for at least 10 reaction runs. The resultant Mo-Co<sub>9</sub>S<sub>8</sub> structure with chemical connection by covalent bonds of Mo-S-Co type on the Co<sub>9</sub>S<sub>8</sub> surface demonstrates strong ability in the adsorption and activation of oxygen-containing substrates, which enables the effective C-O cleavage whilst avoids undesirable hydrogenation of benzene ring. The superior stability and water-resistance at elevated temperature was attributed to the anchoring effect of Al<sub>2</sub>O<sub>3</sub> matrix and “protection” of surface-rich Co<sub>9</sub>S<sub>8</sub> species to the active Mo-Co<sub>9</sub>S<sub>8</sub> center. This strategy provides new insights for the rational design of efficient and stable sulfide catalysts towards the applications in demanding high-temperature reactions.

### 1. Introduction

MoS<sub>2</sub>-based catalysts have been widely used for the removal of hetero-atoms such as sulfur, oxygen and nitrogen from organic molecules in H<sub>2</sub> atmosphere [1,2]. However, one harsh truth is, these sulfide catalysts are unstable due to the sulfur loss under industrial operating conditions [3–5]. Therefore, to promote the practical application of MoS<sub>2</sub>-based catalysts, developing effective strategies to significantly improve their high-temperature stability without sacrificing catalytic activity is desirable.

The catalytic hydrodeoxygenation (HDO) of oxygen-rich biomass into renewable hydrocarbons is becoming more and more important in pursuing a carbon-neutral society [6,7]. It is widely accepted that the

HDO activity of MoS<sub>2</sub> was attributed to the coordinatively unsaturated Mo sites on the edge and/or basal plane with the formation of S vacancies [8–10]. Moreover, previous experimental and theoretical works pointed out that Co doping will increase the availability of vacancy sites by lowering the Mo-S bond energy, which promotes the activation of oxygen in reactants and accelerates proton adsorption [11–13]. Besides, the incorporation of Co at the edge of the MoS<sub>2</sub> sulfide phase increases its stability toward water [14]. Sub-nano catalysts have been widely studied because of their high atom efficiency and distinctive catalytic activity in diverse fields of heterogeneous catalysis [15–17]. Similarly, the strategy of creating Co-Mo interface with atomic Co promoted coordinatively unsaturated Mo sites on MoS<sub>2</sub> edge and/or basal plane should be an effective approach to enhance the catalytic activity as well

\* Corresponding authors.

E-mail addresses: [jina@tju.edu.cn](mailto:jina@tju.edu.cn) (N. Ji), [liuql@tju.edu.cn](mailto:liuql@tju.edu.cn) (Q. Liu), [licz@dicp.ac.cn](mailto:licz@dicp.ac.cn) (C. Li).

<sup>1</sup> These authors contributed equally to this work.



as stability [18]. The state-of-the-art works of the rational design of Co-Mo interface with the formation of Co-substituted S (Mo) sites [3] or Co-MoS<sub>2-x</sub> metal-vacancy [19] have been reported, which focused on achieving high activity under relatively low temperature (< 200 °C) in HDO of lignin-derived model compounds to arenes.

However, unlike simple model compounds, raw lignin possesses much more complicated stubborn structure and an elevated reaction temperature higher than 250 °C is indispensable for MoS<sub>2</sub>-catalyzed lignin conversion [20,21]. According to the literature, significant deactivation of MoS<sub>2</sub>-based catalyst was observed within 4 cycles in various hydrogenation reactions especially under high temperature [11, 22] (Table S1). To our knowledge, in the case of HDO reaction, the deactivation of Co doped MoS<sub>2</sub> catalysts is mainly caused by water, which is in-situ generated by HDO reaction and interacts with active sites at high temperature, resulting in the loss of sulfur from the active Mo sites during the HDO reaction [14,23]. Strategies like built hydrophobic layer on the surface of sulfides have been developed to prevent the adsorption of water on the active sites, which to some extent prevented sulfur loss [24–26].

Inspired by these results, an opposite strategy was proposed: active Co-Mo interfacial sites surrounded by a bunch of groups that readily absorbs water, so that the contact of water with active Co-Mo sites could be avoided. To achieve this indirect protection goal, a Mo doped Co<sub>9</sub>S<sub>8</sub> strategy was proposed. Analogous to the transition-metal doped MoS<sub>2</sub> samples, the transition-metal sulfides (MS<sub>x</sub>, M=Co, Ni, Fe, etc, x > 0) can also be promoted with Mo in MS<sub>x</sub> rich regions in the presence of few MoS<sub>2</sub> slabs [27–29]. Typically, in the case of Mo doped Co<sub>9</sub>S<sub>8</sub>, the coordination environments of Mo atoms would be greatly changed and more coordinatively unsaturated Mo sites will form [30]. Thus, we consider that the rational design of Mo atoms onto the Co<sub>9</sub>S<sub>8</sub> surface with abundant unsaturated Mo sites should possess good HDO activity as well as typical Co-MoS<sub>2</sub> surface. More importantly, the active surface Mo species were surrounded by abundant inert Co<sub>9</sub>S<sub>8</sub> species which would prior to interact with water [31,32].

Herein, a facile synthesis strategy is developed for the fabrication of Mo dispersed on Co<sub>9</sub>S<sub>8</sub>-rich surface (denoted as Mo-Co<sub>9</sub>S<sub>8</sub>/Al<sub>2</sub>O<sub>3</sub>) as a highly selective and robust catalyst that could transform lignin model compounds, lignin bio-oil and even real lignin into arenes. The Mo-Co<sub>9</sub>S<sub>8</sub>/Al<sub>2</sub>O<sub>3</sub> catalyst was prepared by loading Mo on hydrotalcite-derived Co<sub>3</sub>O<sub>4</sub>/Al<sub>2</sub>O<sub>3</sub> and subsequent sulfuration, where the Mo displays in the form of both separated MoS<sub>2</sub> slabs and Mo-Co<sub>9</sub>S<sub>8</sub> structure through chemical connection by covalent bonds of Mo-S-Co type on Co<sub>9</sub>S<sub>8</sub> surface. This multifunctional assembly Mo-Co<sub>9</sub>S<sub>8</sub>/Al<sub>2</sub>O<sub>3</sub> catalyst exhibits electron transfer from Co to Mo sites in Mo-Co<sub>9</sub>S<sub>8</sub> structure, and this Mo-Co<sub>9</sub>S<sub>8</sub> interface has the unique capability for the adsorption of oxygenated compounds, leading to outstanding HDO performance. Moreover, the catalyst displays superior tolerance to high reaction temperature of 265 °C, and resistance against being poisoned by H<sub>2</sub>O, owing to the anchoring effect of Al<sub>2</sub>O<sub>3</sub> matrix and “protection” of Co<sub>9</sub>S<sub>8</sub>. Overall, the work provides a facile strategy for the design of robust molybdenum disulfide catalysts featuring excellent high-temperature stability and HDO activity, highlighting a promise towards the application in demanding high temperature reactions.

## 2. Experimental

### 2.1. Catalyst preparation

#### 2.1.1. Synthesis of the CoAl-LDH precursors

CoAl-LDH precursor with molar ratio of [Co<sup>2+</sup>]/[Al<sup>3+</sup>]= 3/1 was synthesized by a coprecipitation method [4]. In brief, 26.2 g (0.09 mol) Co(NO<sub>3</sub>)<sub>2</sub>.6H<sub>2</sub>O and 11.254 g (0.03 mol) Al(NO<sub>3</sub>)<sub>3</sub>.9 H<sub>2</sub>O, 9.6 g (0.24 mol) NaOH and 6.36 g (0.06 mol) Na<sub>2</sub>CO<sub>3</sub> were dissolved in 250 mL deionized water to form entirely clarified solution, respectively. Subsequently, the two solutions were simultaneously titrated into 500 mL deionized water under continuously stirring and retaining the pH

between 9 and 10 by adjusting the rate of titration. The resulted precipitation solution was further aged at 70 °C for 12 h, then washed with distilled water and then dried at 70 °C overnight.

#### 2.1.2. Synthesis of Mo-Co<sub>9</sub>S<sub>8</sub>/Al<sub>2</sub>O<sub>3</sub> sulfide catalysts

The above-obtained CoAl-LDH precursor was calcined in a muffle oven at 400 °C for 5 h. This calcination process results in the phase transformation of the CoAl-LDH to hydrotalcite-like oxide Co<sub>3</sub>O<sub>4</sub>/Al<sub>2</sub>O<sub>3</sub>. Then, 2.0 g Co<sub>3</sub>O<sub>4</sub>/Al<sub>2</sub>O<sub>3</sub> powder was put into 40 mL aqueous solution with 2.0 g (NH<sub>4</sub>)<sub>6</sub>Mo<sub>7</sub>O<sub>24</sub>, and the mixture was sealed and maintained under stirring for 12 h at room temperature. The obtained MoO<sub>4</sub><sup>2-</sup>-Co<sub>3</sub>O<sub>4</sub>/Al<sub>2</sub>O<sub>3</sub> was washed thoroughly with water and dried in an oven at 70 °C overnight. After the calcination at 400 °C for 5 h (MoO<sub>3</sub>-Co<sub>3</sub>O<sub>4</sub>/Al<sub>2</sub>O<sub>3</sub>) and further sulfidation at 400 °C for 4 h in the flow of H<sub>2</sub>S/H<sub>2</sub> (60 mL/min, Vol(H<sub>2</sub>S)= 10%) with a heating rate of 5 °C/min, the corresponding sample was named as Mo-Co<sub>9</sub>S<sub>8</sub>/Al<sub>2</sub>O<sub>3</sub>.

With the attempt to tailor the surface Mo-Co molar ratio, CoAl-LDH precursors with the Co/Al ratio in the range of 4/1, 3/1, 2/1, 1/1, 1/2 were used, and the final samples were denoted as Mo<sub>x</sub>-Co<sub>9</sub>S<sub>8</sub>/Al<sub>2</sub>O<sub>3</sub> (x refers to the Mo/Co ratio based on ICP analysis).

#### 2.1.3. Synthesis of Co<sub>9</sub>S<sub>8</sub>/Al<sub>2</sub>O<sub>3</sub> and MoS<sub>2</sub>/Al<sub>2</sub>O<sub>3</sub> sulfides

The Co<sub>9</sub>S<sub>8</sub>/Al<sub>2</sub>O<sub>3</sub> was obtained via directly sulfidation of Co<sub>3</sub>O<sub>4</sub>/Al<sub>2</sub>O<sub>3</sub> powder under the same condition as Mo-Co<sub>9</sub>S<sub>8</sub>/Al<sub>2</sub>O<sub>3</sub>. For MoS<sub>2</sub>/Al<sub>2</sub>O<sub>3</sub> synthesis, 5 wt% of Mo was impregnated on Al<sub>2</sub>O<sub>3</sub> support and then the sulfidation was carried out at 400 °C for 4 h in H<sub>2</sub>S/H<sub>2</sub>.

#### 2.1.4. Synthesis of MoS<sub>2</sub> +Co<sub>9</sub>S<sub>8</sub>/Al<sub>2</sub>O<sub>3</sub>-mix

The MoS<sub>2</sub> was synthesized by directly sulfidation of (NH<sub>4</sub>)<sub>6</sub>Mo<sub>7</sub>O<sub>24</sub> under the same condition as Mo<sub>0.06</sub>-Co<sub>9</sub>S<sub>8</sub>/Al<sub>2</sub>O<sub>3</sub>. Then corresponding amount (according to the ICP analysis of Mo<sub>0.06</sub>-Co<sub>9</sub>S<sub>8</sub>/Al<sub>2</sub>O<sub>3</sub>) of MoS<sub>2</sub> and Co<sub>9</sub>S<sub>8</sub>/Al<sub>2</sub>O<sub>3</sub> was physically mixed via grinding for 0.5 h.

#### 2.1.5. Synthesis of conventional supported CoMoS/γ-Al<sub>2</sub>O<sub>3</sub> sulfides

The conventional supported CoMoS/Al<sub>2</sub>O<sub>3</sub> (containing 3 wt% of Co and 10 wt% of Mo) catalysts were prepared as a reference catalyst by the co-impregnation method [33].

## 2.2. Catalyst characterization

X-ray diffraction (XRD) patterns of the samples were collected on a D8-Focus powder diffractometer using Ni-filtered Cu-K $\alpha$  radiation source ( $\lambda$  = 1.54056 Å), with a scan speed of 5°/min and a 20 scan range between 5° and 80°. Nitrogen adsorption measurements were performed on a Micromeritics TriStar surface area and porosity analyzer. The specific surface area and pore size distributions of the samples were determined via nitrogen adsorption using a Micromeritics TriStar surface area and porosity analyzer, and were further calculated by the Brunauer-Emmett-Teller (BET) methods. The bulk composition of the samples was obtained on inductively coupled plasma optical emission spectrometer (ICP-OES), and the samples were completely dissolved by chloroazotic acid with the microwave assistant before test. The morphologies of catalysts were characterized by a Nanosem 430 field emission scanning electron microscope and JEM-2100F transmission electron microscope. X-ray photoelectron spectroscopy (XPS) was performed using a ThermoFisher ESCALAB™ 250Xi spectrometer to characterize the surface chemical property of the samples. Raman spectroscopy (Renishaw Invia) with a Spectra-Physics Excelsior CW solid-state laser ( $\lambda$  = 532 nm) as excitation source was employed to identify the crystalline structure of the samples. The X-ray absorption spectra (XAS) including X-ray absorption near-edge structure (XANES) and extended X-ray absorption fine structure (EXAFS) spectra at the K-edge of Co and Mo were recorded at the BL14W1 at Shanghai Synchrotron Radiation Facility (SSRF), China. The Si (111) and Si (311)-crystal monochromators were used for energy selection for the test of the Co and Mo, respectively. The energy was calibrated by the Co and Mo

foil. The spectra were collected at room temperature under the transmission mode. The data were analyzed by the Athena software packages.

### 2.3. Catalyst test

#### 2.3.1. Catalytic conversion of lignin model compounds

The HDO activity tests were carried out in a 50 mL AB50-C276 reactor (Shanghai LABE Instrument Co., Ltd). Typically, 2.5 mmol lignin model compound, 2.5 mmol dodecane (served as internal standard), 106 mg of catalyst (a mass ratio of 1/4 for catalyst/diphenyl ether) and 20 mL methylcyclohexane (served as solvent) were placed into the autoclave. The autoclave was sealed and the air in the autoclave was evacuated by pressurization–depressurization cycles with H<sub>2</sub> for 5 times, then pressurized with a certain initial pressure of H<sub>2</sub> at ambient temperature. With the mechanical agitation of 800 rpm, the system was heated to the designed temperature and reacted for a certain time. After the reaction, the obtained liquid samples were filtered and qualitatively identified by GC-MS (Agilent 6890A-5975C) to confirm the composition and specific structure of the products. Then we brought the corresponding reagents of GC purity and built the standard curve of each product by the internal standard method based on GC (SP-7890) using a flame ionization detector (FID) with a 30 m WAX capillary column. Thus, the molar concentration of the reactant and products can be quantified on GC (SP-7890), and the conversion and the C6 ring yield for each experiment were calculated as follows:

$$\text{Conversion(Conv. \%)} = \left( 1 - \frac{\text{Mole of residual substrate}}{\text{Mole of initial substrate}} \right) \times 100\% \quad (1)$$

$$\text{Yield}(A, \text{mol}\%) = \frac{\text{Mole of product } A}{\text{Mole of reacted substrate}} \times 100\% \quad (2)$$

The product yield is given relative to the C6 ring because of demethoxylation.

The intrinsic reaction rate of the HDO of diphenyl ether and phenol was calculated assuming a pseudo-first-order reaction as below, with the conversion < 50%.

$$\ln(1-\text{conv.}) = -kt \quad (3)$$

where  $k$  is the pseudo-first-order rate constant (h<sup>-1</sup>), conv. is the conversion of the model compound, and  $t$  is the reaction time (h).

The apparent activation energies ( $E_a$ ) were calculated based on the Arrhenius plots as follows:

$$\ln(k) = (-E_a/RT) + \ln A \quad (4)$$

where  $k$  is the rate constant (h<sup>-1</sup>) at a certain temperature,  $E_a$  is the apparent activation energy (J mol<sup>-1</sup>),  $R$  is the molar gas constant ( $R=8.314 \text{ J mol}^{-1} \text{ K}^{-1}$ ),  $T$  is the reaction temperature (K),  $A$  is the Arrhenius constant (h<sup>-1</sup>).

#### 2.3.2. Catalytic conversion of poplar lignin-oil

The lignin-derived mixture-oil (polar-lignin-oil) used in this paper was prepared according to our previous literature [34]. Here, 50 mg lignin-oil, 100 mg catalyst, 20 mL methylcyclohexane, and 24 mg tridecane (served as internal standard) were sealed in the autoclave, charged with 3 MPa H<sub>2</sub> and stirred at a rate of 800 rpm. The reaction was conducted at 265 °C for 20 h. After the reaction, the obtained liquid sample was qualitatively analyzed by HP 5973 GC-MS using a flame ionization detector (FID) with a 30 m HP-5 capillary column.

#### 2.3.3. Catalytic depolymerization of poplar lignin

The organosolv poplar lignin used in this paper was prepared as described in our previous literature [34]. Here, the autoclave (Parr, 50 mL) was charged with 100 mg organosolv poplar lignin, 200 mg catalyst, 20 mL methylcyclohexane and 24 mg n-tridecane. The reaction condition was the same as that of catalytic conversion of poplar

lignin-oil. After the reaction, the mixture was filtered and the filtrate was concentrated naturally at atmospheric pressure to obtain the liquid oil product, which was further weighed. The liquid product was then diluted to 2 mL with methylcyclohexane solvent, and the monomer products in the liquid oil were analyzed and quantified by HP 5973 GC-MS using a flame ionization detector (FID) with a 30 m HP-5 capillary column. Conversion and the yield of each product were calculated as follows:

$$\text{Carbon yield}(A, \text{wt. \%}) = \left( \frac{[C]_A * m_A}{[C]_i * m_i} \right) \times 100 \text{ wt.\%} \quad (5)$$

$$\text{Total Carbon yield (wt.\%)} = \sum_i^x \text{carbon yield (A}_i\text{)} \quad (6)$$

with  $m$  representing the mass,  $[C]$  representing the mass fraction of carbon,  $A$  the product,  $i$  the initial lignin.

#### 2.3.4. Catalyst recycle

The spent catalyst was collected after the reaction and washed with ethanol for several times. After drying at 120 °C for 12 h, the recycled catalyst was directly used for the next reaction cycle.

### 2.4. Density functional theory calculations

#### 2.4.1. Computational details

The density-functional theory (DFT) calculations were performed using the Vienna Ab-initio Simulation Package (VASP) to get molecular-level understanding of the reaction mechanism. In this work, the Blöchl's all-electron-like projector augmented plane wave (PAW, the Perdew-Burke-Ernzerhof (PBE) functional, a cutoff energy of 500 eV, and a  $4 \times 4 \times 1$  Monkhorst-Pack grid k-points were used. The structures were optimized until the energy and the force were converged to  $1.0 \times 10^{-5}$  eV/atom and 0.02 eV/Å, respectively. A vacuum space as large as 15 Å was used along the c direction normal to the catalyst surface to avoid periodic interactions.

#### 2.4.2. Computational surface models

The MoS<sub>2</sub> (001) surface model with the layer S atoms exposed and the S-terminated Co<sub>9</sub>S<sub>8</sub> (100) surface model were built, as is shown in Figs. S1 and 2. Co located on the Mo atop site of MoS<sub>2</sub> slabs with  $4 \times 4$  periodicities was set as Co-MoS<sub>2</sub> (001) model, which was constructed for comparison according to a previous study of Co<sup>8</sup>MoS<sub>2</sub> (001) [3]. The Mo-Co<sub>9</sub>S<sub>8</sub> (100) surface model in this work was structured based on the above XAS characterization results via constant optimization, and it resembled a recent study of Mo-Co<sub>9</sub>S<sub>8</sub> @C catalyst [30].

Based on the computational surface models, we performed a primary DFT calculation on adsorption of diphenyl ether and phenol on these models, respectively. The specific calculation formula of adsorption energy is as follows.

$$E_{\text{ads}} = E_{\text{Surface-Reactant}} - (E_{\text{Surface}} + E_{\text{Reactant}}) \quad (7)$$

Where  $E_{\text{Surface-Reactant}}$  is the total energy of the system reactant (diphenyl ether or phenol) adsorbed on the corresponding surface,  $E_{\text{Reactant}}$  is the total energy of a single reactant molecule in the vacuum,  $E_{\text{Surface}}$  is the total energy of the corresponding surface.

## 3. Results and discussion

### 3.1. Preparation and textual properties of Mo-Co<sub>9</sub>S<sub>8</sub>/Al<sub>2</sub>O<sub>3</sub> catalyst

Fig. 1a shows the typical synthetic scheme of the Mo anchoring on the surface of Co<sub>9</sub>S<sub>8</sub>, denoted as Mo-Co<sub>9</sub>S<sub>8</sub>/Al<sub>2</sub>O<sub>3</sub>. Firstly, small and immobilized Co<sub>3</sub>O<sub>4</sub> NPs are generated on the Al<sub>2</sub>O<sub>3</sub> matrix based on the structural topotactic transformation of CoAl layered double hydroxide (LDH) [35,36]. Subsequently, the Mo precursor is decorated on the

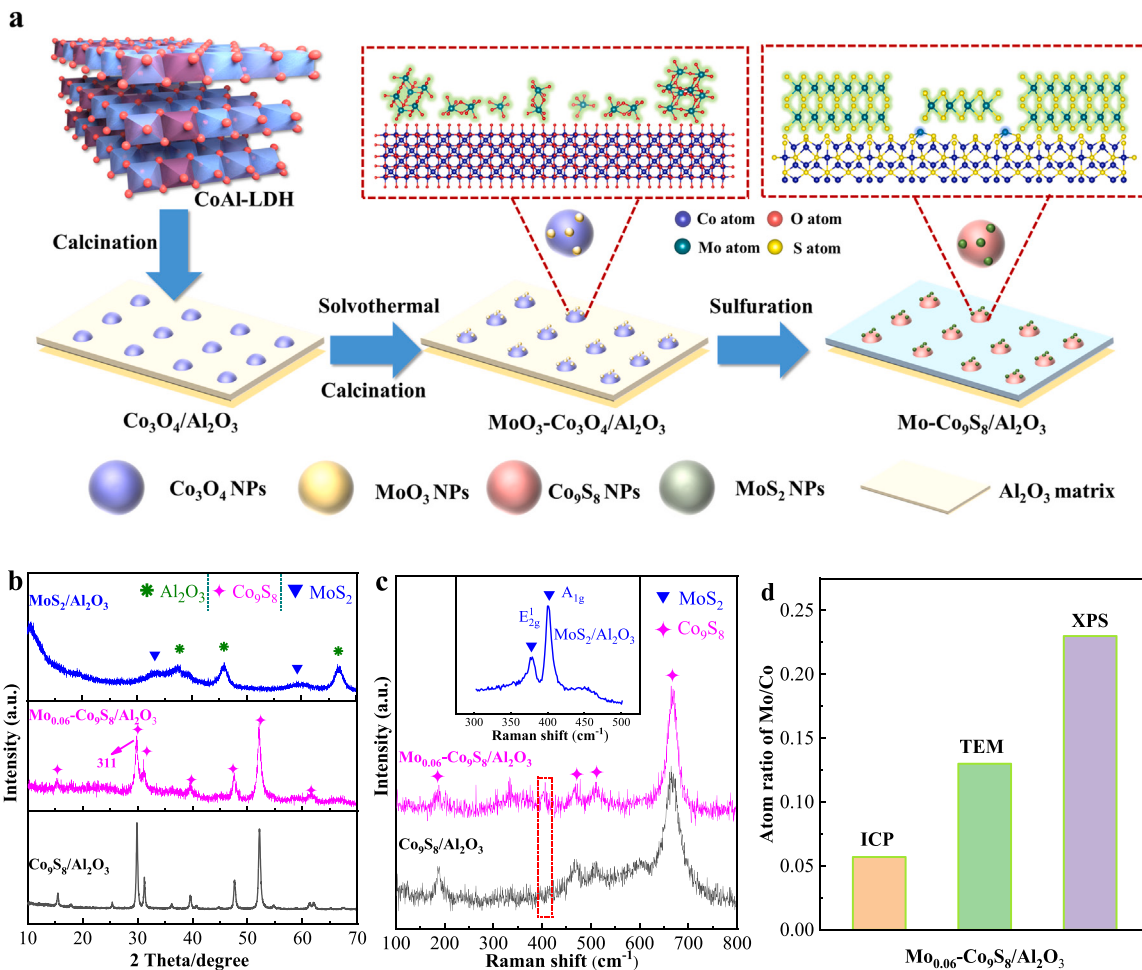


**Fig. 1.** (a) Schematic illustration of the preparation procedure of Mo-Co<sub>9</sub>S<sub>8</sub>/Al<sub>2</sub>O<sub>3</sub> catalyst. (b) XRD patterns, (c) Raman spectra of Mo<sub>0.06</sub>-Co<sub>9</sub>S<sub>8</sub>/Al<sub>2</sub>O<sub>3</sub>, Co<sub>9</sub>S<sub>8</sub>/Al<sub>2</sub>O<sub>3</sub>, and MoS<sub>2</sub>/Al<sub>2</sub>O<sub>3</sub>. (d) Atom ratio of Mo/Co obtained by ICP, TEM, and XPS.

surface of Co<sub>3</sub>O<sub>4</sub> via the solvothermal method and simultaneously transformed into sulfides after sulfuration in the flow of H<sub>2</sub>S/H<sub>2</sub>. The Mo/Co ratio in Mo-Co<sub>9</sub>S<sub>8</sub>/Al<sub>2</sub>O<sub>3</sub> can be facilely controlled by tuning the Co/Al molar ratio of the parent CoAl-LDH, and denoted as

Mo<sub>x</sub>-Co<sub>9</sub>S<sub>8</sub>/Al<sub>2</sub>O<sub>3</sub> (x refers to the Mo/Co molar ratio, which was estimated by ICP-OES). The optimal value of Mo/Co molar ratio is found to be 0.06 and the as-synthesized Mo<sub>0.06</sub>-Co<sub>9</sub>S<sub>8</sub>/Al<sub>2</sub>O<sub>3</sub> shows typical layered morphology with the specific surface area of 18.9 m<sup>2</sup>/g and

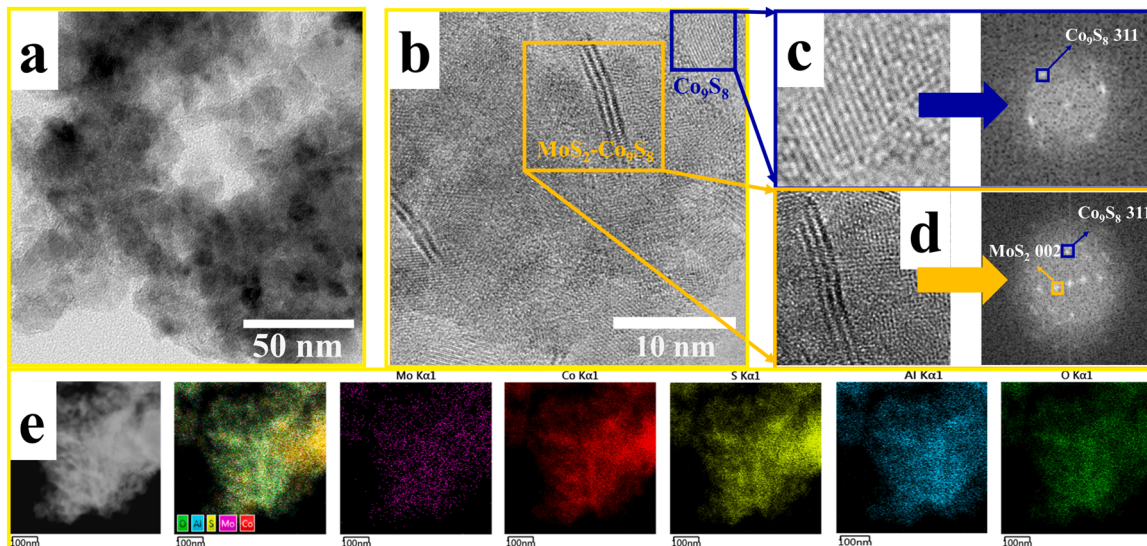


**Fig. 2.** (a) TEM image, and (b) HRTEM image for Mo<sub>0.06</sub>-Co<sub>9</sub>S<sub>8</sub>/Al<sub>2</sub>O<sub>3</sub>. (c) Magnified image and FFT analysis for Co<sub>9</sub>S<sub>8</sub> (311). (d) Magnified image and FFT analysis for MoS<sub>2</sub> (002). (e) TEM-EDX mapping of Co, Mo, S, Al, and O elements.

mesoporous structure (Figs. S3 and 4, and Tables S2 and 3).

The X-ray diffraction (XRD) patterns of  $\text{Mo}_{x}\text{-Co}_9\text{S}_8/\text{Al}_2\text{O}_3$  showed typical peaks for  $\text{Co}_9\text{S}_8$  phase (JCPDS 65–6801); no characteristic peaks for  $\text{MoS}_2$  were observed in XRD, probably because of low loading and/or high dispersion of Mo element (Fig. 1b and Fig. S3c) [37]. The weak signals of distinctive  $\text{MoS}_2$  vibrational peaks (the  $\text{E}_{1\ 2g}$  (in-plane) and  $\text{A}_{1g}$  (out-of-plane) modes [38,39]) for  $\text{Mo}_{0.06}\text{-Co}_9\text{S}_8/\text{Al}_2\text{O}_3$  in Raman spectroscopy agrees well with the XRD characterization (Fig. 1c). The chemical composition of  $\text{Mo}_{0.06}\text{-Co}_9\text{S}_8/\text{Al}_2\text{O}_3$  was characterized by ICP, TEM-EDS, and XPS. As shown in Fig. 1d, the surface Mo/Co molar ratio ( $\approx 0.23$  for XPS and  $\approx 0.13$  for STEM-EDX) is much higher than that of the bulk ( $\approx 0.06$  for ICP). Such surface enrichment of Mo claimed that most Mo atoms prefer the dispersion on  $\text{Co}_9\text{S}_8$  surface. High-resolution transmission electron microscopy (HRTEM) was performed to inspect the detailed structure of the catalysts. As shown in Fig. S5a-b, the  $\text{Co}_3\text{O}_4$  NPs are successfully anchored on the  $\text{Al}_2\text{O}_3$  matrix in  $\text{Co}_3\text{O}_4/\text{Al}_2\text{O}_3$ . The characteristic lattice fringe of the (311) plane of cubic  $\text{Co}_9\text{S}_8$  are presented in images of both  $\text{Co}_9\text{S}_8/\text{Al}_2\text{O}_3$  and  $\text{Mo}_{0.06}\text{-Co}_9\text{S}_8/\text{Al}_2\text{O}_3$  (Fig. 2c and Fig. S3c-d), implying that the surface Mo modification does not alter the cubic crystal phase, which is consistent with XRD and Raman results. In addition, the typical (002) lattice fringes and corresponding FFT of  $\text{MoS}_2$  sheet are also confirmed by high-resolution scan in Fig. 2d, suggesting the presence of few-layered separated  $\text{MoS}_2$  slabs on the surface of  $\text{Co}_9\text{S}_8$ . To identify the elements' distribution, energy dispersive X-ray spectroscopy (EDX) mapping is employed. The Mo elements are uniformly distributed along with the Co, S, Al, and O elements, demonstrating the evenly dispersion of Mo on  $\text{Co}_9\text{S}_8$  surface. (Fig. 2e).

### 3.2. Probing into the electronic and coordinative structure

X-ray photoelectron spectroscopy (XPS) was conducted to determine the valence state of surface Co, Mo and S species. As shown in Fig. 3a, the Co 2p spectra are fitted with three doublets: the first one at 778.2 eV from  $\text{Co}^{3+}$ , the second one at 781.2 eV from  $\text{Co}^{2+}$ , and the third one from broadened peak satellite signals, which are in accordance with the previous reported  $\text{Co}_9\text{S}_8$  characteristic peaks [40,41]. The Mo 3d spectra in  $\text{Mo}\text{-Co}_9\text{S}_8/\text{Al}_2\text{O}_3$  can be mainly deconvoluted into two peaks

(Fig. 3d),  $\text{Mo 3d}_{5/2}$  (239.1 eV) and  $\text{Mo 3d}_{3/2}$  (232.9 eV), illustrating the existence of  $\text{Mo}^{4+}$  in Mo-S bond and  $\text{Mo}^{6+}$  in Mo-O bond. Compared to  $\text{Co}_9\text{S}_8/\text{Al}_2\text{O}_3$  and  $\text{MoS}_2/\text{Al}_2\text{O}_3$ , the positive shift in Co-S peaks (Co 2p<sub>3/2</sub> 778.4–778.5 eV) and the negative shift in Mo-S peaks (Mo 3d<sub>5/2</sub> 229.2–229.1 eV) in  $\text{Mo}_{0.06}\text{-Co}_9\text{S}_8/\text{Al}_2\text{O}_3$  implies the electron transfer from Co to Mo sites (Fig. 3d), which suggest the formation of Mo on  $\text{Co}_9\text{S}_8$  surface by the bridging S. Additionally, the proportion of  $\text{Co}^{3+}$  increases remarkably ( $\text{Co}^{3+}/\text{Co}^{2+}=0.46$ ) in Co 2p spectra for  $\text{Mo}_{0.06}\text{-Co}_9\text{S}_8/\text{Al}_2\text{O}_3$  when compared to  $\text{Co}_9\text{S}_8/\text{Al}_2\text{O}_3$  ( $\text{Co}^{3+}/\text{Co}^{2+}=0.19$ ) (Table S4). These results confirm the strong interaction between Mo and Co atoms with the increased electron density at the Mo site. For S 2s spectra, two peaks at 226.3 and 227.2 eV which corresponding to Co-S and Mo-S species, respectively, were observed in  $\text{Mo}_{0.06}\text{-Co}_9\text{S}_8/\text{Al}_2\text{O}_3$  catalyst, further suggesting the Mo-Co strong interaction. Moreover, the peaks at 162.5 and 163.7 eV in S 2p spectra (Fig. S7) are attributed to S 2p<sub>3/2</sub> and S 2p<sub>1/2</sub> orbitals of divalent sulfide ions ( $\text{S}^{2-}$ ), which agrees well with the formation of Mo-S bond. And the other two S 2p peaks at 161.7 and 162.9 eV are assigned to S 2p<sub>3/2</sub> and S 2p<sub>1/2</sub> of Co-S bonding in  $\text{Co}_9\text{S}_8$  crystals, respectively [42]. It is interesting to note that the ratios of  $\text{Co}^{3+}/\text{Co}^{2+}$  and  $\text{Mo}^{4+}/\text{Mo}^{6+}$  reached the maximum in  $\text{Mo}_{0.06}\text{-Co}_9\text{S}_8/\text{Al}_2\text{O}_3$  (Fig. S8 and Table S4), suggesting its strongest Mo-Co interaction.

X-ray absorption near-edge structure (XANES) and extended X-ray absorption fine structure (EXAFS) measurements were employed to further investigate the structural characteristics of the catalyst. The Co K-edge XANES spectra of  $\text{Co}_9\text{S}_8/\text{Al}_2\text{O}_3$  and  $\text{Mo}_{0.06}\text{-Co}_9\text{S}_8/\text{Al}_2\text{O}_3$  along with those of standard Co sulfide and Co foil are shown in Fig. 3b. It can be observed that the Co K absorption edge (7710–7718 eV) of the  $\text{Mo}_{0.06}\text{-Co}_9\text{S}_8/\text{Al}_2\text{O}_3$  shifts toward the higher energy compared to pure  $\text{Co}_9\text{S}_8$  and  $\text{Co}_9\text{S}_8/\text{Al}_2\text{O}_3$ , demonstrating more highly-changed  $\text{Co}^{3+}$  was formed because of the Mo-Co interaction [27,43]. Moreover, it is reported that the high pre-edge intensity (7710 eV) of  $\text{Co}_9\text{S}_8$  is a characteristic feature of eight tetrahedral Co sites in the unit cell of  $\text{Co}_9\text{S}_8$  ( $\text{Fm-3 m}$ ) with low symmetry, whereas the  $\text{CoS}_2$  ( $\text{Pa-3}$ ) comprises only octahedral Co site showed rather lower pre-edge intensity with high symmetry (Fig. S9b) [44]. Therefore, the significantly lower 1 s-3d pre-edge peak intensity at 7710 eV for  $\text{Mo}_{0.06}\text{-Co}_9\text{S}_8/\text{Al}_2\text{O}_3$  (0.090) than

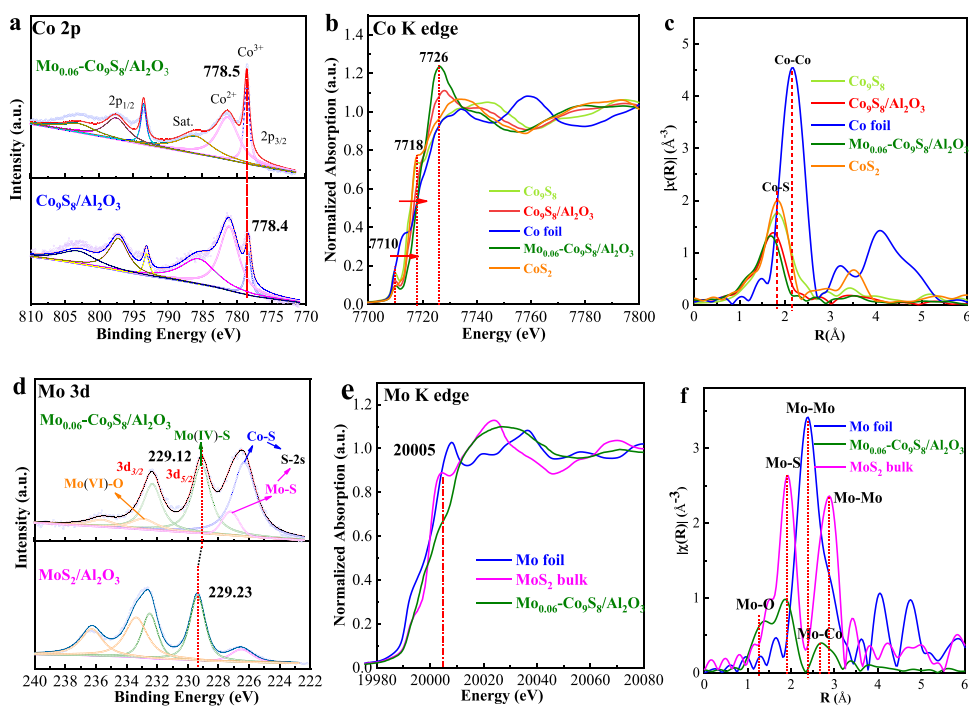


Fig. 3. (a) XP spectra for Co 2p. (b-c) XANES and EXAFS spectra of Co K-edge, respectively. (d) XP spectra for Mo 3d. (e-f) XANES and EXAFS spectra of Mo K-edge, respectively.

that for  $\text{Co}_9\text{S}_8/\text{Al}_2\text{O}_3$  (0.124) (Fig. S9a) suggests a higher symmetric structure of Co atoms in  $\text{Mo}-\text{Co}_9\text{S}_8$  than in  $\text{Co}_9\text{S}_8$  [11,45]. Fig. 3c displays the Fourier transform of the EXAFS spectra at Co K edge. The major peak for  $\text{Mo}_{0.06}-\text{Co}_9\text{S}_8/\text{Al}_2\text{O}_3$  at 1.69 Å verifies the dominant first shell Co-S contribution, and no Co-Mo contribution can be observed. In conclusion, the Co atoms in  $\text{Mo}_{0.06}-\text{Co}_9\text{S}_8/\text{Al}_2\text{O}_3$  catalyst mainly exist as  $\text{Co}_9\text{S}_8$  phase, and exhibit a significant enhanced symmetry and valence state by the surface promotion of Mo atoms.

The Mo K edge XANES spectrum for the bulk  $\text{MoS}_2$  shows a distinct pre-edge feature at 20005 eV, which corresponding to the forbidden transition from 1s to 4d levels [46,47], while not detected for  $\text{Mo}_{0.06}-\text{Co}_9\text{S}_8/\text{Al}_2\text{O}_3$  (Fig. 3e). This suggests the Mo local coordination environment in  $\text{Mo}_{0.06}-\text{Co}_9\text{S}_8/\text{Al}_2\text{O}_3$  is different from that of  $\text{MoS}_2$  phase. The Mo K-edge EXAFS spectrum of bulk  $\text{MoS}_2$  in Fig. 3f shows two peaks denoting Mo-S ( $R=3.15$  Å) and Mo-Mo ( $R=2.40$  Å) bond corresponding to six Mo-S and six Mo-Mo. Distinctly decreased intensity for Mo-S and Mo-Mo peaks are observed in  $\text{Mo}_{0.06}-\text{Co}_9\text{S}_8/\text{Al}_2\text{O}_3$ . Quantitative analysis for Mo K-edge in Table 1 shows that the Debye-Waller factor noticeably increase for Mo-S in  $\text{Mo}_{0.06}-\text{Co}_9\text{S}_8/\text{Al}_2\text{O}_3$ , which indicates more structural disorder of Mo-S bond was formed in  $\text{Mo}_{0.06}-\text{Co}_9\text{S}_8/\text{Al}_2\text{O}_3$  [43]. Interestingly, an evident second shell of Mo-Co rather than Mo-Mo contribution centered at 2.68 Å was detected, implying the doping of Mo atoms in the form of Mo-S-Co bond [44,48]. The measured coordination numbers ( $\text{CN}_{\text{Mo-S}}=3.3$ ) together with Mo species in Mo-S-Co bond point to the sulfur deficient Mo sites in  $\text{Mo}_{0.06}-\text{Co}_9\text{S}_8/\text{Al}_2\text{O}_3$ . According to literature, the Mo-S coordination numbers in Co doped  $\text{MoS}_2$  (CoMoS phase or  $\text{Co}_9\text{S}_8-\text{MoS}_2$  heterostructure) only showed a slight decrease ( $\text{CN}_{\text{Mo-S}}\approx 5.5$ ) [43,44], whereas the formation of  $\text{Mo}_4\text{S}_4$  cluster or  $\text{MoFe}_3\text{S}_3\text{C}$  subunit leads to an evident decline of  $\text{CN}_{\text{Mo-S}}$  to about 3 due to the exposure of unsaturated Mo atoms [49,50]. Therefore, we hypothesize that in this Mo-S-Co structure, the Mo atom is coordinated to three bridging S atoms on the top site of  $\text{Co}_9\text{S}_8$ , resulting in theoretical  $\text{CN}_{\text{Mo-S}}=3$  (signed as  $\text{Mo}-\text{Co}_9\text{S}_8$  center) (Fig. S9b). Slightly higher measured coordination numbers ( $\text{CN}_{\text{Mo-S}}=3.3$ ) are attributed to a minor presence of a few  $\text{MoS}_2$  slabs on the surface of  $\text{Co}_9\text{S}_8$ , as observed by HRTEM in Fig. 2b. The Mo doped  $\text{Co}_9\text{S}_8$  model was further deduced by the density functional theory (DFT) and details are described in the section of mechanistic study.

Table 1

The Mo K-edge EXAFS results for fresh and spent  $\text{Mo}_{0.06}-\text{Co}_9\text{S}_8/\text{Al}_2\text{O}_3$ .  $\text{CN}_{\text{Mo-S}}$  and  $\text{R}_{\text{Mo-S}}$  of bulk  $\text{MoS}_2$  and other typical  $\text{MoS}_2$  materials from literature are added for comparison.

Sample	Shell	$\text{CN}^a$	$R$ (Å) <sup>b</sup>	$\sigma^2$ ( $\times 10^{-2}$ Å <sup>2</sup> ) <sup>c</sup>	$\Delta E_0$ (eV) <sup>d</sup>	r-factor (%) <sup>e</sup>
Bulk $\text{MoS}_2$	Mo-Mo	6.0	3.15	0.47	-3.2	0.1
	Mo-S	6.0	2.40	0.21	0.7	
$\text{Mo}_{0.06}-\text{Co}_9\text{S}_8/\text{Al}_2\text{O}_3$	Mo-S	3.3	2.40	0.59	-11.0	0.2
After 1 run	Mo-S	3.1	2.40	0.62	-10.3	0.1
$\text{Co}_9\text{S}_8-\text{MoS}_2$ [43]	Mo-S	5.5	2.41	0.31	-	0.15
$\text{Co}_{0.2}\text{Mo}_{0.8}\text{S}$ [44]	Mo-S	5.5	2.42	0.60	-	-
$\text{Mo}_4\text{S}_4$ cluster [49]	Mo-S	2.6	2.47	0.55	-	0.04
$\text{MoFe}_3\text{S}_3\text{C}$ [50]	Mo-S	3.0	2.32	-	-	-

<sup>a</sup> Coordination number for the absorber-back scatterer pair.

<sup>b</sup> Average absorber-back scatterer distance.

<sup>c</sup> Debye-Waller factor.

<sup>d</sup> Inner potential correction.

<sup>e</sup> A sum of squares measure of the fractional misfit. The accuracies of the above parameters were estimated as  $\text{CN}$ ,  $\pm 20\%$ ;  $R$ ,  $\pm 1\%$ ;  $\sigma^2$ ,  $\pm 20\%$ ;  $\Delta E_0$ ,  $\pm 20\%$ . The  $\Delta k$  (3.0–12.8 Å<sup>-1</sup>) and  $\Delta R$  (1.1–2.3 Å) are the data ranges used for data fitting in k-space and R-space, respectively.

### 3.3. Catalytic performance of $\text{Mo}-\text{Co}_9\text{S}_8/\text{Al}_2\text{O}_3$ catalysts in HDO reaction

The catalytic activities of the catalysts were tested by HDO of diphenyl ether (DPE), considering that resistant 4-O-5 linkage is one of the most abundant C-O bonds in lignin and the target product benzene is widely used in the manufacture of value-added chemicals. Listed in Table 2 are the results obtained from blank experiment and catalyst screening. Entry 1 shows that a 2.1% conversion of DPE was achieved in a blank experiment in absence of any catalyst. This result indicates that the substrate is thermally stable at 300 °C due to its relatively high bond dissociation energy. With the presence of  $\text{MoS}_2$ ,  $\text{Al}_2\text{O}_3$ ,  $\text{MoS}_2/\text{Al}_2\text{O}_3$  or  $\text{Co}_9\text{S}_8/\text{Al}_2\text{O}_3$ , only trace target benzene was detected under 4.0 MPa H<sub>2</sub> at 300 °C for 4 h (Table 2, entries 2–5), suggesting the negligible HDO activity of single  $\text{Al}_2\text{O}_3$  matrix and the monometallic  $\text{MoS}_2$  or  $\text{Co}_9\text{S}_8$  phase. After engineering Mo anchored on  $\text{Co}_9\text{S}_8$ , the formation of Mo-Co interface significantly improved the HDO activity (Table 2, entries 6–10). Among the  $\text{Mo}_x-\text{Co}_9\text{S}_8/\text{Al}_2\text{O}_3$  with different Mo/Co ratios,  $\text{Mo}_{0.06}-\text{Co}_9\text{S}_8/\text{Al}_2\text{O}_3$  with the highest  $\text{Co}^{3+}$  and  $\text{Mo}^{4+}$  proportion presented the maximum HDO activity, providing a benzene yield up to 87.2% (Table 2, entry 9). As Mo species displayed in the form of a few  $\text{MoS}_2$  slabs and major  $\text{Mo}-\text{Co}_9\text{S}_8$  structure in  $\text{Mo}_{0.06}-\text{Co}_9\text{S}_8/\text{Al}_2\text{O}_3$  catalyst, simply mixed  $\text{MoS}_2$  +  $\text{Co}_9\text{S}_8/\text{Al}_2\text{O}_3$ -Mix sample with separated  $\text{MoS}_2$  slabs on  $\text{Co}_9\text{S}_8/\text{Al}_2\text{O}_3$  were prepared and tested for catalyzing HDO of DPE (Table 2, entry 11). As expected, it only affords a 10.4% yield of benzene, unequivocally demonstrating that the catalytic activity of  $\text{Mo}_{0.06}-\text{Co}_9\text{S}_8/\text{Al}_2\text{O}_3$  from DPE to benzene can mainly be ascribed to the  $\text{Mo}-\text{Co}_9\text{S}_8$  structure.

We further investigated the HDO activity of  $\text{Mo}_{0.06}-\text{Co}_9\text{S}_8/\text{Al}_2\text{O}_3$  at different reaction temperatures. As shown in Table 2 entries 12–16, when the temperature is dropped to 250 °C, the conversion rate decreases remarkably although the reaction time was prolonged to 10 h. The conversion of DPE to benzene seems to be a temperature-sensitive reaction. When the temperature reached 265 °C,  $\text{Mo}_{0.06}-\text{Co}_9\text{S}_8/\text{Al}_2\text{O}_3$  afforded 99.8% conversion with benzene yield of 91.0% (Table 2, entry 12), which was much higher than that of  $\text{CoMoS}/\text{Al}_2\text{O}_3$  catalyst prepared by traditional impregnation method with typical  $\text{CoMoS}$  phase (Table 2, entry 17). Lower or higher temperatures would cause incomplete reaction or over-hydrogenation of the aromatic ring. The effect of catalyst dosage and initial H<sub>2</sub> pressure was also investigated (Fig. S10), and the reaction condition of 106 mg catalyst (catalyst dosage/DPE mass=1/4), 265 °C, 3 MPa H<sub>2</sub>, and 10 h becomes the optimized condition. In comparison with previous reported investigations (Table S5),  $\text{Mo}_{0.06}-\text{Co}_9\text{S}_8/\text{Al}_2\text{O}_3$  catalyst present comparable HDO reactivity ( $Y_{\text{benzene}}=91.0\%$ ) to the state-of-the-art such as Raney Ni/H-BEA-35 ( $Y_{\text{benzene}}=84.4\%$ ) [51] and Ru-WO<sub>x</sub>/ZrO<sub>2</sub> ( $Y_{\text{benzene}}=95.7\%$ ) [52] in the transformation of DPE into benzene.

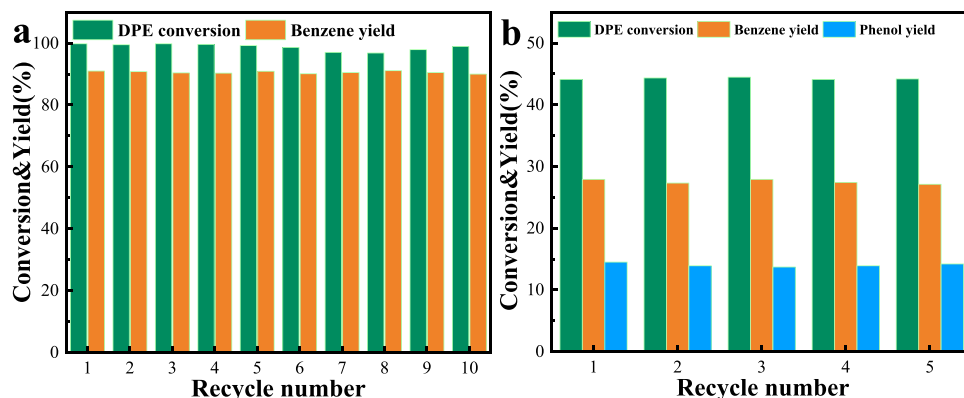
### 3.4. Recyclability and water-resistance of the catalyst

The recyclability of  $\text{Mo}_{0.06}-\text{Co}_9\text{S}_8/\text{Al}_2\text{O}_3$  catalyst was investigated by catalyzing DPE to benzene, and the results are shown in Fig. 4. After the HDO reaction at 265 °C for 10 cycles, the conversion and benzene yield remained at about 99.8% and 91.0%, respectively (Fig. 4a), presenting no obvious deactivation. When reaction time was shortened to 2 h, the DPE conversion and benzene yield remained at about 44.5% and 27.5% for 5 cycles (Fig. 4b), respectively. If the catalyst dosage was reduced from 106 mg to 43 mg, the DPE conversion and benzene yield remained at about 95.0% and 76.0% for 4 cycles (Fig. S11), respectively. These results fully demonstrate that  $\text{Mo}_{0.06}-\text{Co}_9\text{S}_8/\text{Al}_2\text{O}_3$  exhibited excellent stability at elevated temperature, which shows a clear breakthrough when compared with the former  $\text{MoS}_2$ -based catalysts (Table S1).

Characterizations of the spent  $\text{Mo}_{0.06}-\text{Co}_9\text{S}_8/\text{Al}_2\text{O}_3$  after reaction at 265 °C for 10 h in different runs gave direct evidence on the stability. The spent  $\text{Mo}_{0.06}-\text{Co}_9\text{S}_8/\text{Al}_2\text{O}_3$  catalysts almost had the same XRD and Raman pattern as that of the fresh catalyst (Fig. 5a-b), and the crystal size also remained almost unchanged although after 10 runs (Table S6),

**Table 2**Conversion of DPE over different sulfide catalysts.<sup>a</sup>

Entry	Catalyst	DPE			Benzene	Phenol	Cyclohexane	Mythycyclopentane	Phenylcyclohexane	6 f	
		1a			2b	3c	4d	5e	6f		
		T (°C)	P (MPa)	t (h)	Conv. (%)	Yield (%)	2b	3c	4d	5e	
1	Blank	300	4	4	2.1		1.0	0.9	0	0	0
2	Al <sub>2</sub> O <sub>3</sub>	300	4	4	3.1		1.5	1.3	0	0	0
3	MoS <sub>2</sub>	300	4	4	4.5		2.9	1.9	0	0	0
4	Mo <sub>0.2</sub> /Al <sub>2</sub> O <sub>3</sub>	300	4	4	11.9		5.9	4.4	0	0	0
5	Co <sub>9</sub> S <sub>8</sub> /Al <sub>2</sub> O <sub>3</sub>	300	4	4	5.7		3.3	2.2	0	0	0
6	Mo <sub>0.1</sub> -Co <sub>9</sub> S <sub>8</sub> /Al <sub>2</sub> O <sub>3</sub>	300	4	4	89.3		62.9	12.3	9.5	0.7	2.0
7	Mo <sub>0.09</sub> -Co <sub>9</sub> S <sub>8</sub> /Al <sub>2</sub> O <sub>3</sub>	300	4	4	97.3		73.7	9.2	9.4	1.0	3.3
8	Mo <sub>0.07</sub> -Co <sub>9</sub> S <sub>8</sub> /Al <sub>2</sub> O <sub>3</sub>	300	4	4	97.3		76.4	8.6	6.8	1.0	3.3
9	Mo <sub>0.06</sub> -Co <sub>9</sub> S <sub>8</sub> /Al <sub>2</sub> O <sub>3</sub>	300	4	4	98.9		87.2	5.7	4.1	0.3	1.8
10	Mo <sub>0.05</sub> -Co <sub>9</sub> S <sub>8</sub> /Al <sub>2</sub> O <sub>3</sub>	300	4	4	98.4		83.2	7.7	6.0	0.1	1.5
11	Mo <sub>0.05</sub> -Co <sub>9</sub> S <sub>8</sub> /Al <sub>2</sub> O <sub>3</sub> -Mix	300	4	4	33.5		10.4	22.1	0	0	0
12	Mo <sub>0.06</sub> -Co <sub>9</sub> S <sub>8</sub> /Al <sub>2</sub> O <sub>3</sub>	250	3	10	80.7		65.0	11.3	3.0	0	1.2
13	Mo <sub>0.06</sub> -Co <sub>9</sub> S <sub>8</sub> /Al <sub>2</sub> O <sub>3</sub>	255	3	10	92.6		79.4	8.4	3.4	0.2	1.2
14	Mo <sub>0.06</sub> -Co <sub>9</sub> S <sub>8</sub> /Al <sub>2</sub> O <sub>3</sub>	260	3	10	98.8		86.7	6.8	3.9	0.1	1.4
15	Mo <sub>0.06</sub> -Co <sub>9</sub> S <sub>8</sub> /Al <sub>2</sub> O <sub>3</sub>	265	3	10	99.4		91.0	2.0	4.1	0.5	1.9
16	Mo <sub>0.06</sub> -Co <sub>9</sub> S <sub>8</sub> /Al <sub>2</sub> O <sub>3</sub>	270	3	10	99.8		80.9	0.7	11.1	0.9	6.2
17	CoMoS/Al <sub>2</sub> O <sub>3</sub> <sup>b</sup>	265	3	10	84.9		62.2	13.5	5.0	0.2	2.4

<sup>a</sup> Reaction conditions: DPE 426 mg (2.5 mmol), catalyst 106 mg, solvent methylcyclohexane 20 mL.<sup>b</sup> Prepared by impregnation method.**Fig. 4.** (a) Stability test of  $\text{Mo}_{0.06}\text{-Co}_9\text{S}_8/\text{Al}_2\text{O}_3$  in the HDO of DPE at  $265\text{ }^\circ\text{C}$  for 10 h. (b) Stability test of  $\text{Mo}_{0.06}\text{-Co}_9\text{S}_8/\text{Al}_2\text{O}_3$  in the HDO of DPE at  $265\text{ }^\circ\text{C}$  for 2 h.

indicating that the  $\text{Co}_9\text{S}_8$  particles are well anchored on the  $\text{Al}_2\text{O}_3$  matrix without any phase transition. The TEM results also showed that no obvious agglomeration of  $\text{Co}_9\text{S}_8$  particles was observed, further demonstrated the anchoring effect of  $\text{Al}_2\text{O}_3$  to  $\text{Co}_9\text{S}_8$  (Fig. 5c). ICP analysis in Table S6 showed that the Co/Mo/S content of  $\text{Mo}_{0.06}\text{-Co}_9\text{S}_8/\text{Al}_2\text{O}_3$  catalyst only presented little decline after reaction for 10 runs, which agrees well with the above characterizations. The XANES and EXAFS spectra of Co and Mo K edge also almost keep unchanged before or after the reaction, suggesting that the coordination environment of Mo and Co holds steady (Fig. 5d-g). All the results demonstrated that  $\text{Mo}_{0.06}\text{-Co}_9\text{S}_8/\text{Al}_2\text{O}_3$  exhibited high stability in the bulk structure during the HDO reaction. However, XPS results showed that the surface proportion of Co-S bond in S 2p and S 2s presented apparent decline after reaction (Fig. 5h,j and Table S7), indicating that the surface  $\text{Co}_9\text{S}_8$  species underwent significant change in chemical state. In contrast, the proportion of  $\text{Mo}^{4+}$  in Mo 3d displayed no obvious change and the proportion of Mo-S bond in S 2p increased remarkably after reaction (Fig. 5i and Table S6). Therefore, we inferred that only the surface  $\text{Co}_9\text{S}_8$

species underwent a significant change in chemical state, whereas the surface Mo active center and the bulk structure of the catalyst remained stable without obvious change after the reaction.

To further understand the intrinsic reason for the chemical state change of Co species and the stabilization mechanism of the catalyst during the reaction, the HDO of DPE over  $\text{Mo}_{0.06}\text{-Co}_9\text{S}_8/\text{Al}_2\text{O}_3$  in the presence of water was carried out. In our work, a total of 45 mg water will be generated if the O in DPE (2.5 mmol) was completely removed. Therefore, reactions with enlarged water addition (250–1500 mg) were performed under the same reaction conditions. As shown in Fig. 6a, the appropriate addition of water leads to a small increase in the benzene yield, which is in accordance with the previous works [23]. Excessive water (1500 mg) would cause the competitive adsorption between water and DPE on active sites, and then decrease the conversion and benzene yield. The XRD patterns of these recovered catalysts illustrated that the main phase change from  $\text{Co}_9\text{S}_8$  to cobalt sulfate hydrate phase, and the intensity of cobalt sulfate hydrate increased with the presence of more water addition (run 1) (Fig. 6b). This indicates that

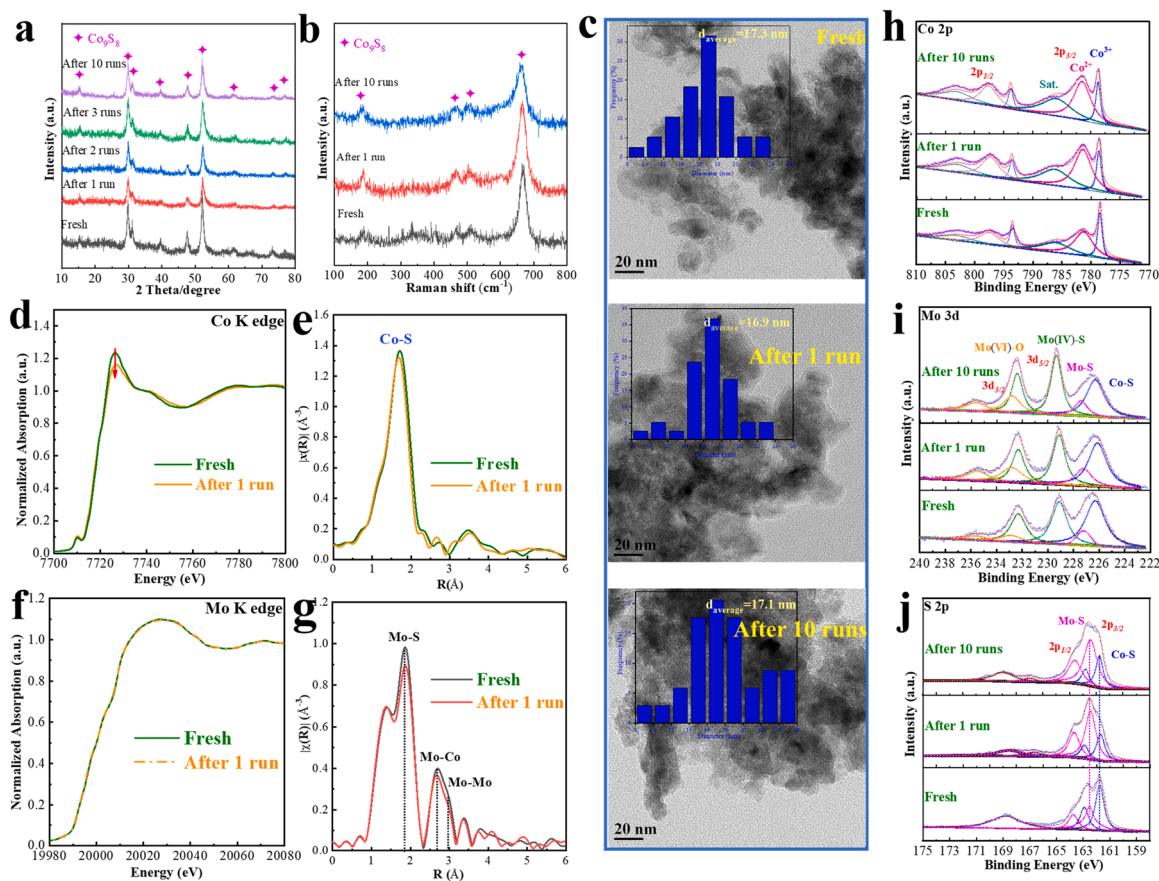


**Fig. 5.** Characterizations of the spent  $\text{Mo}_{0.06}\text{-Co}_9\text{S}_8/\text{Al}_2\text{O}_3$  catalysts. (a) XRD patterns. (b) Raman patterns. (c) TEM images, with the insets showing the particle size distribution of  $\text{Co}_9\text{S}_8$  NPs. (d-e) XANES and EXAFS spectra of Co K-edge, respectively. (f-g) XANES and EXAFS spectra of Mo K-edge, respectively. (h-j) XP spectra of Co 2p, Mo 3d, and S 2p, respectively.

$\text{Co}_9\text{S}_8$  species indeed reacted with the water during the HDO reaction. Fig. 6c displays the HDO results over the recovered  $\text{Mo}_{0.06}\text{-Co}_9\text{S}_8/\text{Al}_2\text{O}_3$  catalysts from the former water addition system. It can be seen that the recovered catalyst with the main phase of cobalt sulfate hydrate presented a small increase in the benzene yield, and all the catalysts turned back to the  $\text{Co}_9\text{S}_8$  phase after reaction (run 2) (Fig. 6d). In conclusion, with the presence of enlarged quantities of water, the surface-rich  $\text{Co}_9\text{S}_8$  species are passivated preferentially and translated to cobalt sulfate hydrate, whereas the active  $\text{Mo}\text{-Co}_9\text{S}_8$  center remains almost unchanged ascribe to the protection of  $\text{Co}_9\text{S}_8$  (Fig. 6e).

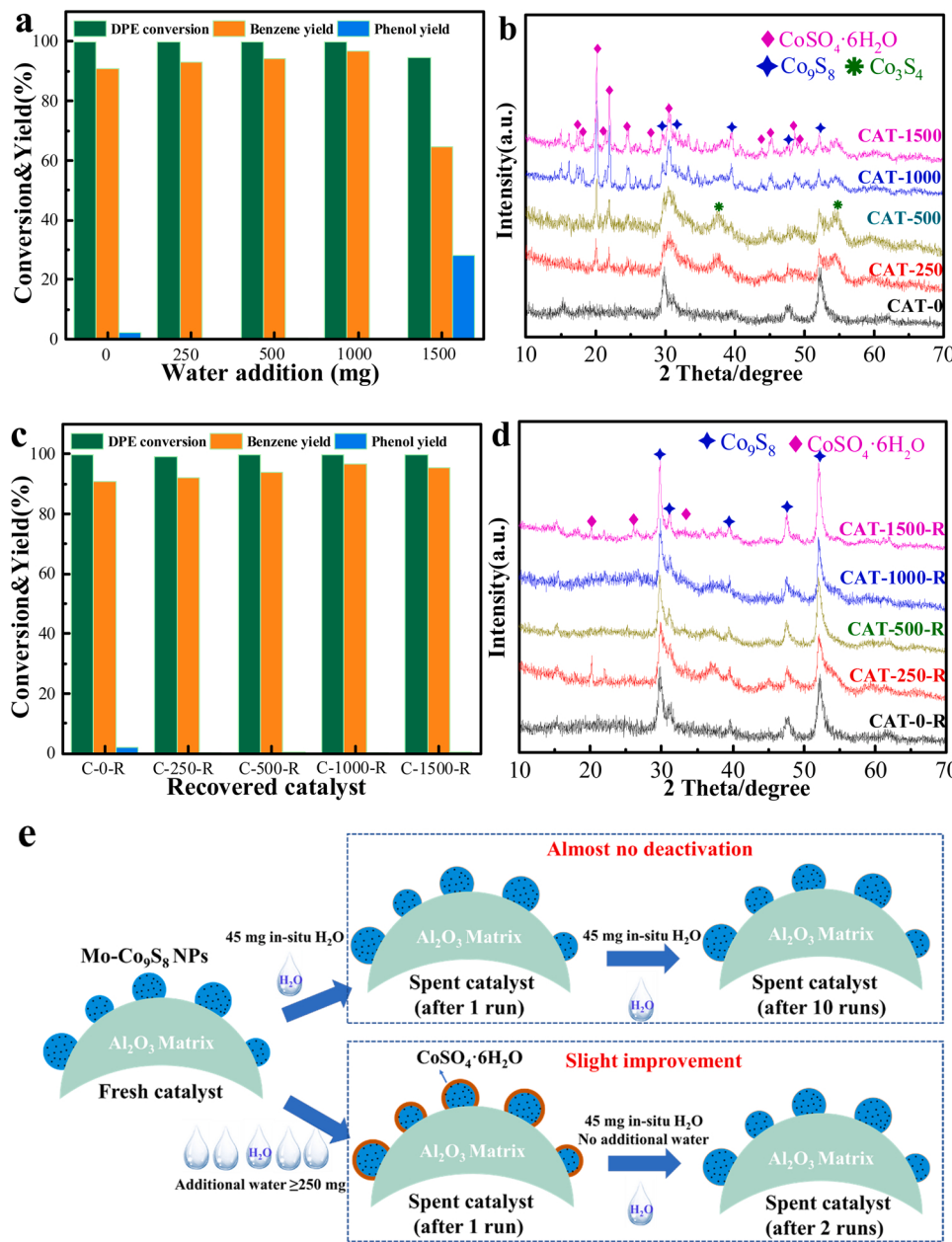
### 3.5. HDO of lignin-derived monomers, dimers and oil

To investigate the applicability of  $\text{Mo}_{0.06}\text{-Co}_9\text{S}_8/\text{Al}_2\text{O}_3$  catalyst, different lignin-derived monomers, dimers and even lignin-oil were evaluated under 3 MPa  $\text{H}_2$  at 265 °C. As shown in Table 3, for the phenolic compounds with  $\text{C}_{\text{Ar}}\text{-OH}$  ( $\text{BDEs} = 447.0 \text{ kJ mol}^{-1}$ ) linkage [53], such as phenol, *p*-cresol, 4-ethylphenol and 4-propylphenol, the yields of arenes were all close to 90.0%, while the conversion and cycloalkanes selectivity slightly increased due to the influence of the additional alkyl groups on para-position (Table 3, entries 1–4). Similar result was obtained on benzyl alcohol and anisole (Table 3, entries 5–6), albeit they have different oxygen-containing groups. Comparatively, when the number of the side-chain oxygen-containing group increased, such as catechol, guaiacol and veratrole, prolonged reaction time is necessary for maximum the oxygen removal rate. In this case, the yield of benzene decreased (~60–70%) and more cycloalkanes were generated (~20–30%) (Table 3, entries 7–10). Nevertheless, high deoxygenation was achieved for all above model compounds. More importantly,

when the poplar lignin-oil with various oxygen-containing monomers was applied to the HDO reaction, the oxygen was also almost removed, providing arenes and alkylated arenes as the main products (Fig. S12), along with a considerable amount of cycloalkanes. For dimer model compounds dibenzyl ether ( $\alpha\text{-O}$  linkage), 99.4% conversion was achieved and the yield of toluene was 86.1% (Table 3, entry 11). Likewise, the HDO of diphenyl ether ( $\alpha\text{-O-4}$  linkage,  $\text{BDEs} = 218.1 \text{ kJ mol}^{-1}$ ) [54] presented 95.5% conversion with toluene and benzene yields of 83.4% and 81.8%, respectively (Table 3, entry 12). When additional methyl group exists on ortho-position of DPE, the conversion was 95.9% and accompanied by the formation of toluene and benzene with a yield of 87.9% and 85.2%, respectively (Table 3, entry 13). For 2-(2-methoxyphenoxy)-1-phenylethanol ( $\beta\text{-O-4}$  linkage,  $\text{BDEs} = 289.0 \text{ kJ mol}^{-1}$ ) [55], 82.0% yield of benzene and 93.0% yield of ethylbenzene was achieved (Table 3, entry 14). Notably, For the  $\beta\text{-O-4}$  model compound with  $\gamma\text{-OH}$ , which represents a typical realistic segment of lignin, an 99.9% conversion was achieved with dominated arene products (Table 3, entry 15). Almost all monomers, dimers and even lignin-oil were converted into arenes with selective cleavage of C–O bond, suggesting that  $\text{Mo}_{0.06}\text{-Co}_9\text{S}_8/\text{Al}_2\text{O}_3$  catalyst exhibited an excellent HDO activity and arene selectivity.

### 3.6. HDO of poplar lignin

Given the excellent HDO activity obtained on model compounds and lignin-oil, we further investigated the catalytic depolymerization performance of organosolv poplar lignin over  $\text{Mo}_{0.06}\text{-Co}_9\text{S}_8/\text{Al}_2\text{O}_3$  catalyst. Fig. 7 illustrates the product distribution and yield of monomer products based on GC-MS characterization. To our delight, no phenolics were



detected in the monomers, implying that the catalyst is also highly selective in C-O hydrogenolysis even in the depolymerization of real lignin. The total carbon yield of monomers was 14.8 wt%, including 9.1 wt% of arenes and 5.6 wt% of cycloalkanes. It is consistent with the results on model compounds with 61.9% selectivity of arenes in the monomers.

Besides the quantitative monomers according to GC, the composition of the remaining oil components was further determined by 2D-HSQC NMR spectra, and the comparison of lignin and corresponding oil products was displayed in Fig. 8. For the side-chain region, it was found that the cross signals of C-O at  $\delta_{\text{C}}/\delta_{\text{H}} = 50\text{--}90/2.5\text{--}6$  ppm were observed in the lignin before reaction, which represents the correlations of  $\beta\text{-O-4}$ ,  $\beta\text{-5}$ ,  $\alpha\text{-O-4}$  and  $\beta\text{-}\beta$ , as shown in the structure A, B, C. After the reaction, almost no A, B, C linkages were observed in the side-chain region of the oil, illustrating the high efficiency of  $\text{Mo}_{0.06}\text{-Co}_9\text{S}_8/\text{Al}_2\text{O}_3$  for the cleavage of these C-O linkages. For the aromatic region, typical signals at  $\delta_{\text{C}}/\delta_{\text{H}} = 100\text{--}140/6\text{--}8$  ppm are represented for the S, G, H and PB types of aromatic structure. The absence of these signals and the

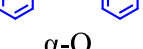
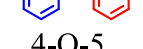
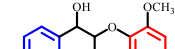
retainment of aromatic signals for lignin oil confirmed that the oxygen species on the side-chain were almost removed while the benzene ring remained. Moreover, for the  $\text{Csp}^3\text{-H}$  region at  $\delta_{\text{C}}/\delta_{\text{H}} = 10\text{--}50/0\text{--}2.5$  ppm, the signals on lignin oil enhanced because of the further formation of over hydrogenated products and the replacement of O by H when the C-O bonds broke. These results suggested that the as-obtained oil mainly consisted of arenes and cycloalkanes, which was in agreement with the lignin oil conversion results. All these results demonstrated that  $\text{Mo}_{0.06}\text{-Co}_9\text{S}_8/\text{Al}_2\text{O}_3$  possessed high activity and selectivity, unrivalled stability and resistance against being poisoned by  $\text{H}_2\text{O}$ , as well as excellent tolerance to a wide spectrum of lignin model compounds and realistic lignin, which is of great potential for practical applications.

### 3.7. Mechanistic study

Control experiments, kinetic studies, and DFT calculations were performed to get insight into the reaction mechanism of  $\text{Mo}\text{-Co}_9\text{S}_8/\text{Al}_2\text{O}_3$ -catalyzed HDO reaction of DPE. It is worth noting that the HDO of

Table 3

HDO of various lignin monomers and dimers over  $\text{Mo}_{0.06}\text{-Co}_9\text{S}_8/\text{Al}_2\text{O}_3$  catalyst.<sup>a</sup>

Entry	Substrates	Conv. (%)	$\text{C}_6$ ring yield (%)	
			Arenes	Cycloalkanes
1		95.7	 89.6	 3.2
2		98.2	 89.2	--
3		97.8	 88.1	 8.9
4		99.7	 87.9	 10.7
5		96.5	 89.4	--
6		99.7	 80.1	 5.9
7 <sup>b</sup>		99.8	 72.4	 19.4
8 <sup>b</sup>		99.5	 67.3	 3.7
9 <sup>b</sup>		99.8	 74.6	 3.4
10 <sup>b</sup>		99.5	 60.0	 3.6
11	 $\alpha$ -O	99.4	 86.1	--
12	 $\alpha$ -O-4	95.5	 81.8	 83.4
13	 4-O-5	95.9	 85.2	 87.9
14 <sup>c</sup>	 $\beta$ -O-4	99.9	 93.0	 82.0
15 <sup>c</sup>	 $\beta$ -O-4	99.9	 8.6	 24.6
			 6.5	 61.5
				 6.4

<sup>b</sup>20 h.<sup>c</sup>Substrate 100 mg, catalyst 100 mg.

<sup>a</sup> Reaction conditions: reactant 426 mg (2.5 mmol), catalyst 106 mg, methylcyclohexane 20 mL, 265 °C, 3 MPa H<sub>2</sub>, 10 h.

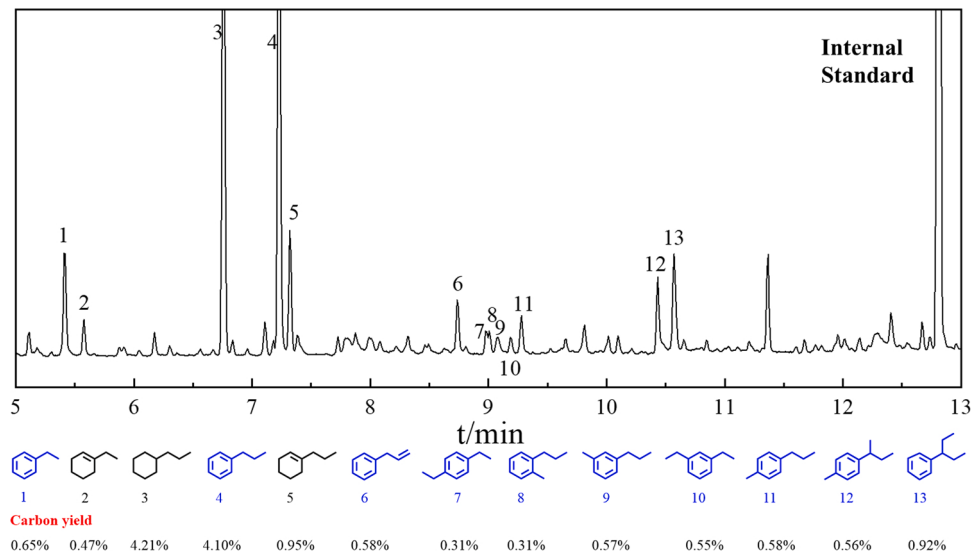


**Fig. 7.** GC-MS results and carbon yield of monomer products. Reaction conditions: Organosolv poplar lignin (100 mg), Mo<sub>0.06</sub>-Co<sub>9</sub>S<sub>8</sub>/Al<sub>2</sub>O<sub>3</sub> catalyst (200 mg), methylcyclohexane (20 mL), n-tridecane (24 mg), temperature (265 °C), pressure (3 MPa), H<sub>2</sub>, time (20 h). Elemental composition of poplar lignin: [C]= 56.95 wt%, [O]= 36.591 wt%, [H]= 6.459 wt%.

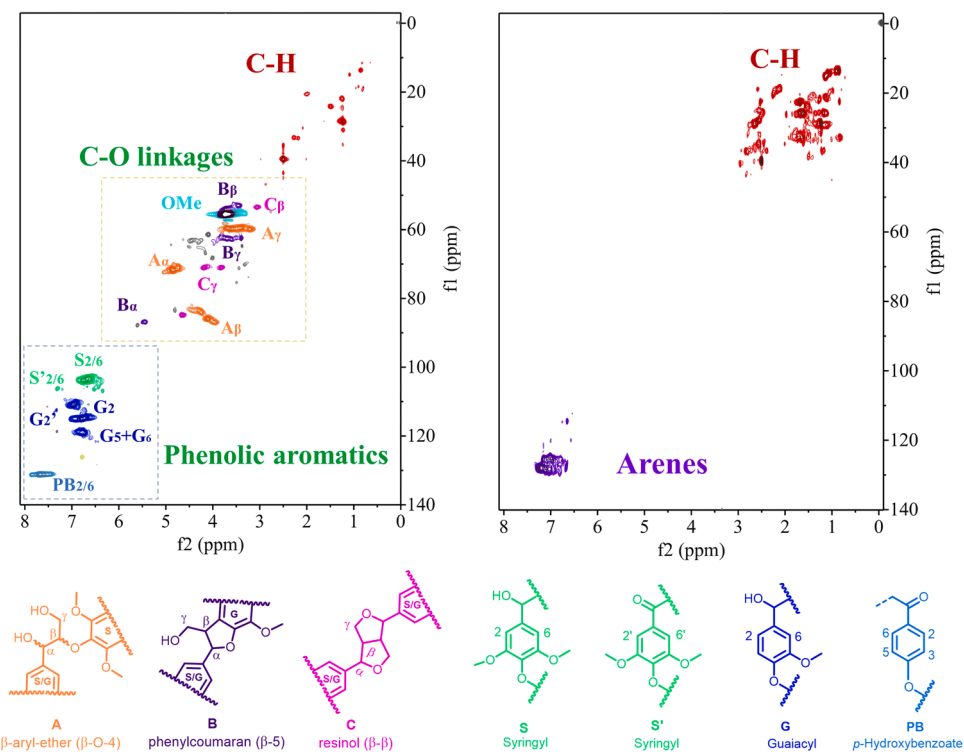
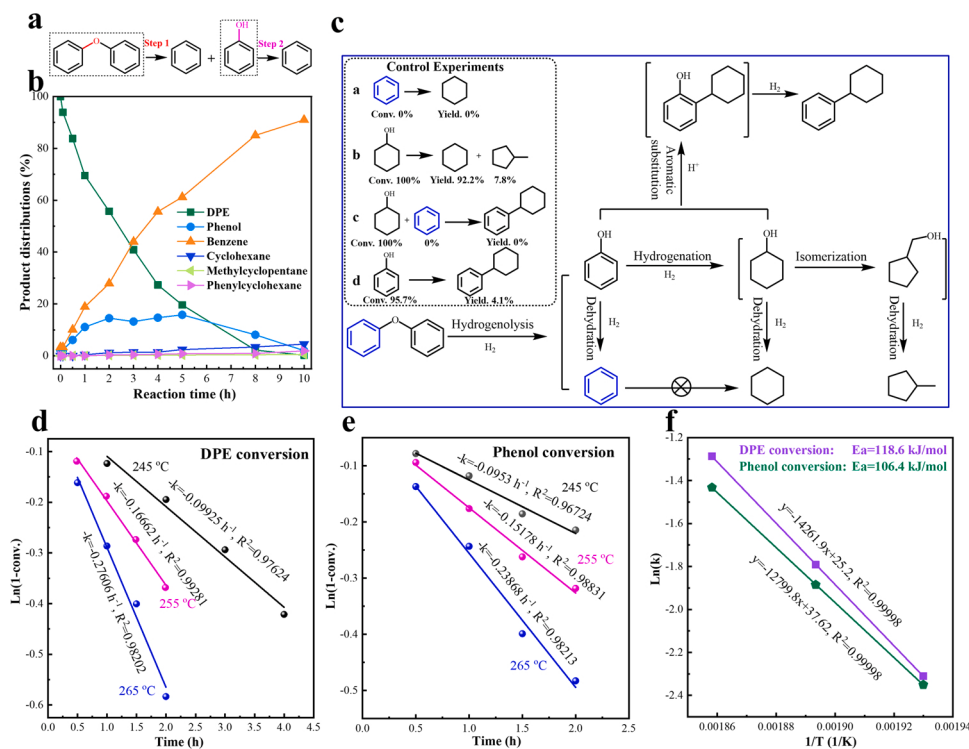


**Fig. 8.** 2D-HSQC analyze of organosolv poplar lignin (left), and oil products from lignin degradation over Mo<sub>0.06</sub>-Co<sub>9</sub>S<sub>8</sub>/Al<sub>2</sub>O<sub>3</sub> (right).

DPE to benzene need to firstly overcome the cleavage of the strongest aryl-aryl ether linkage (4-O-5 bond) and then remove the phenolic hydroxyl group (Ph-OH bond) via deoxygenation [53], as shown in Fig. 9a.

In our case, the initial DPE and subsequent generated phenol were gradually converted to benzene with the extension of reaction time, and no dicyclohexyl ether or cyclohexyl phenyl ether was detected, indicating that Mo-Co<sub>9</sub>S<sub>8</sub>/Al<sub>2</sub>O<sub>3</sub> catalyst could selectively cleave 4-O-5 bond before hydrogenating the aromatic ring (Fig. 9b). Trace by-products

were detected as cyclohexane, methylcyclopentane and phenylcyclohexane. The formation mechanism of the by-products was explored according to the control experiments performed over Mo<sub>0.06</sub>-Co<sub>9</sub>S<sub>8</sub>/Al<sub>2</sub>O<sub>3</sub> catalyst. Using benzene as a substrate under the same reaction condition afforded no conversion (Reaction (a) in Fig. 9c), indicated that benzene as the final product was stable in this catalytic system. According to the literature, the hydrogenation of phenol will lead to the formation of cyclohexanol, and cyclohexanol can be easily converted to



cyclohexane and methylcyclopentane. To ascertain this route, the conversion of cyclohexanol was carried out (Reaction (b) in Fig. 9c), and the cyclohexanol was completely converted with the formation of cyclohexane (Yield=92.2%) and methylcyclopentane (Yield=7.8%). Thus we proposed that trace methylcyclopentane was probably generated from the cyclopentanemethanol, which was isomerized from cyclohexanol. It is reported that the presence of cyclohexanol can be act as an alkylating agent [56]. The comparison of Reaction (c) and (d) in Fig. 9c indicated that the electrophilic aromatic substitution of cyclohexanol occurred on the aromatic ring of phenol with the formation of cyclohexyl-phenol, which further translated to phenylcyclohexane via deoxygenation. Therefore, the whole transformation of DPE is proposed in Fig. 9c.

On the basis of the above results, the cleavage of the 4-O-5 and phenolic C-O bond should be the key step to benzene production. We next attempted to explore the relation of the thermodynamic properties of the C-O bond to the kinetic parameters. (Fig. 9d,e) showed a first-order linear relationship of  $\ln(1-\text{conv.})$  with the reaction time for the hydrogenolysis of DPE and phenol conversion at low conversion. In principle, the cleavage of phenolic C-O bond in phenol should be more difficult than that of 4-O-5 bond in DPE ( $\text{BDE}=314 \text{ kJ}\cdot\text{mol}^{-1}$ ), as it has much higher BDE ( $447 \text{ kJ}\cdot\text{mol}^{-1}$ ) [53]. The results showed that the reaction rate for 4-O-5 was a bit higher than that for phenolic C-O with the  $\text{Mo}_{0.06}\text{-Co}_9\text{S}_8/\text{Al}_2\text{O}_3$  catalyst (Table 4), which agrees with the fact that it has lower BDE. However, the further calculations based on the

**Fig. 9.** (a) Key step for the HDO of DPE to benzene. (b) Product distributions as a function of reaction time for the  $\text{Mo}_{0.06}\text{-Co}_9\text{S}_8/\text{Al}_2\text{O}_3$  catalyst. Reaction conditions: DPE 426 mg,  $\text{Mo}_{0.06}\text{-Co}_9\text{S}_8/\text{Al}_2\text{O}_3$  106 mg, 3 MPa  $\text{H}_2$ , 265 °C. (c) Proposed reaction pathway for the HDO of DPE (diphenyl ether) over  $\text{Mo}_{0.06}\text{-Co}_9\text{S}_8/\text{Al}_2\text{O}_3$  catalyst, with the insets showing the control experiments. (d-e) First-order kinetic fit for DPE and phenol conversion at different temperatures, respectively. (f) Arrhenius plots of DPE and phenol conversion, respectively.

Arrhenius plots showed that the apparent activation energy ( $E_a$ ) of the DPE conversion ( $118.6 \text{ kJ}\cdot\text{mol}^{-1}$ ) was higher than that of phenol ( $106.4 \text{ kJ}\cdot\text{mol}^{-1}$ ) (Fig. 9f). This may be attributed to that the DPE conversion is an overall reaction including both the 4-O-5 cleavage and the further phenolic C-O cleavage. Nevertheless, it should be noted that  $\text{Mo}_{0.06}\text{-Co}_9\text{S}_8/\text{Al}_2\text{O}_3$  catalyst had high activity for the C-O cleavage with relatively low apparent activation energy.

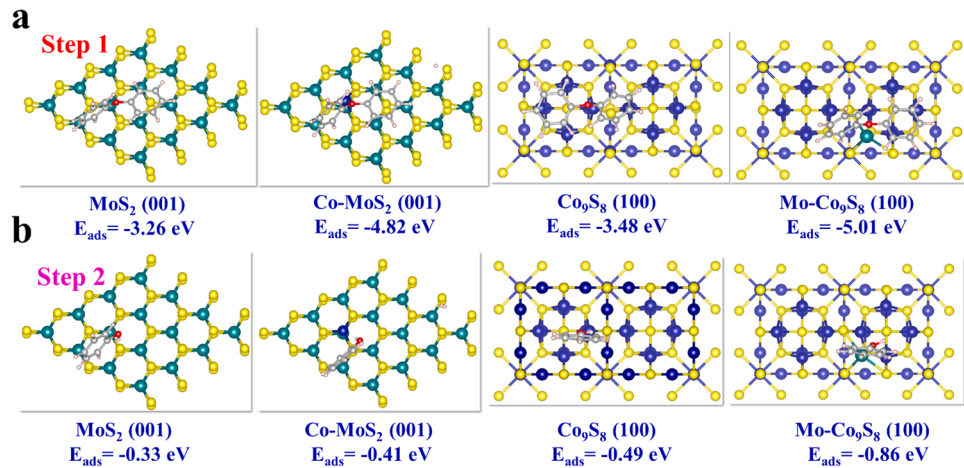
It is accepted that the first step for the heterogeneous reaction is the chemical adsorption of the functional group. Therefore, to further understand the reaction mechanism in molecular-level and the intrinsic reason for the high HDO activity of  $\text{Mo}\text{-Co}_9\text{S}_8/\text{Al}_2\text{O}_3$ , DFT calculations were carried out to investigate the adsorption of DPE and phenol molecules on the surface of catalysts (Fig. 10 and Tables S8 and 9). The typical  $\text{Co}\text{-MoS}_2$  surface model with Co located on the Mo atop site was structured according to the previous work [3], while the  $\text{Mo}\text{-Co}_9\text{S}_8$  surface model with Mo atom coordinates to three bridging S atoms on the top site of  $\text{Co}_9\text{S}_8$  was structured based on the above characterization results via constant optimization. The results showed that either Co doping on  $\text{MoS}_2$  or Mo doping on  $\text{Co}_9\text{S}_8$  greatly improved the vertical adsorption of oxygenated compounds, which enables the effective C-O cleavage whilst avoids undesirable hydrogenation of benzene ring. Especially, the  $\text{Mo}\text{-Co}_9\text{S}_8$  surface ( $-5.01 \text{ eV}$ ) exhibits even lower adsorption energy of DPE than that of  $\text{Co}\text{-MoS}_2$  surface ( $-4.82 \text{ eV}$ ), which indicated that the  $\text{Mo}\text{-Co}_9\text{S}_8$  surface facilitated the adsorption and

Table 4

Bond dissociation energies (BDEs), reaction rate constants, and apparent activation energies ( $E_a$ ) for DPE and phenol conversion to benzene.

Entry	Substrate	Linkage	BDE (kJ mol <sup>-1</sup> )	Reaction rate (h <sup>-1</sup> ) <sup>a</sup>			$E_a$ (kJ mol <sup>-1</sup> )
				245 °C	255 °C	265 °C	
1		4-O-5	314.0	0.09925	0.16662	0.27606	118.6
2		C <sub>Ar</sub> -OH	447.0	0.0953	0.15178	0.23868	106.4

<sup>a</sup> Reaction conditions: reactant 2.5 mmol, catalyst 106 mg, methylcyclohexane 20 mL, 265 °C, 3 MPa  $\text{H}_2$ , reaction time was adjusted to achieve conversion < 50%.



**Fig. 10.** (a) DFT calculation for the adsorption of DPE on different surfaces. (b) DFT calculation for the adsorption of phenol on different surfaces. The yellow, green, red, grey and white spheres represented S, Mo, Co, O and H atoms, respectively.

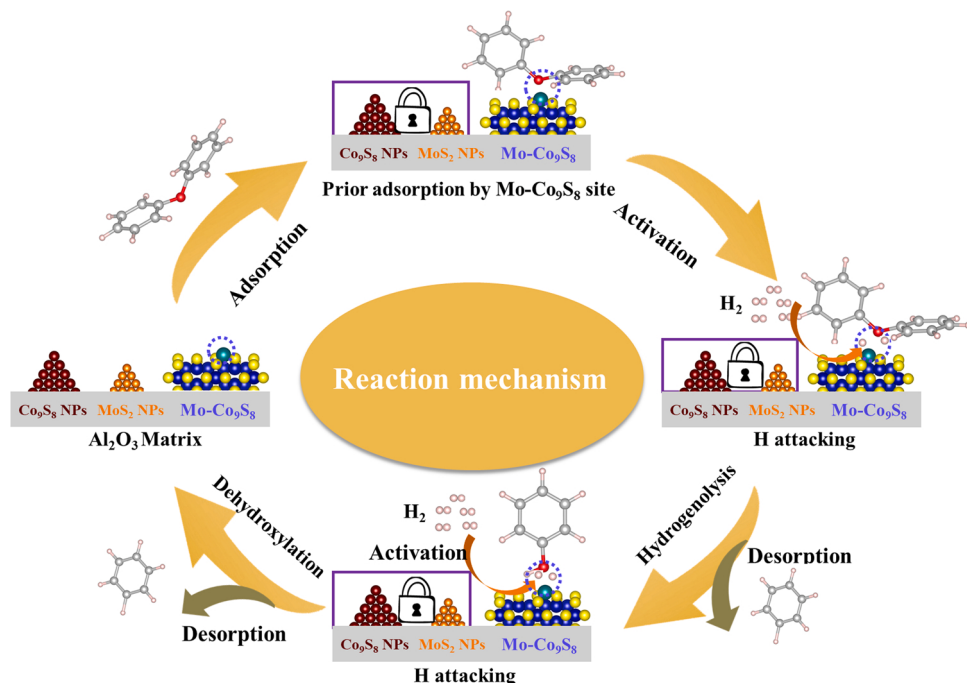
activation of C-O bond in DPE. It should be noticed that the adsorption of DPE is much easier than that of phenol on Mo-Co<sub>9</sub>S<sub>8</sub> site, which agrees well with the fact that DPE has a relative higher reaction rate. These DFT calculation results indicate that the Mo-Co<sub>9</sub>S<sub>8</sub> structure in Mo-Co<sub>9</sub>S<sub>8</sub>/Al<sub>2</sub>O<sub>3</sub> served as active center for the adsorption and activation of oxygen functional groups in DPE and phenol.

Based on the discussion above, the proposed catalytic mechanism of DPE HDO over Mo-Co<sub>9</sub>S<sub>8</sub>/Al<sub>2</sub>O<sub>3</sub> was illustrated in **Scheme 1**. In order to demonstrate this process clearly, the MoS<sub>2</sub>, Co<sub>9</sub>S<sub>8</sub> and Mo-Co<sub>9</sub>S<sub>8</sub> sites were depicted separately. The electronegative carbonyl oxygen in DPE was firstly adsorbed by unsaturation Mo site at Mo-Co<sub>9</sub>S<sub>8</sub> surface, which weakened the C-O bond. The electronic transfer from Co to Mo in Mo-Co<sub>9</sub>S<sub>8</sub> sites resulted in a high activity for hydrogen dissociation [19], thus the dissociated H species generated at Mo-Co<sub>9</sub>S<sub>8</sub> sites attacked the C-O group, leading to the cleavage of 4-O-5 bond to form phenol and benzene. The generated phenol subsequently underwent a similar adsorption and activation processes, then formed benzene via deoxygenation. The MoS<sub>2</sub> and Co<sub>9</sub>S<sub>8</sub> sites acted as nearly inert center for the

reactant adsorption and hydrogen dissociation with low activity. The outstanding activity of Mo-Co<sub>9</sub>S<sub>8</sub>/Al<sub>2</sub>O<sub>3</sub> catalyst was attributed to the formation of Mo-Co<sub>9</sub>S<sub>8</sub> hybrid phase and electronic transfer from Co to Mo, which enhanced the O-contained group adsorption ability and accelerated the dissociation of hydrogen, respectively.

#### 4. Conclusion

In summary, we have fabricated highly active, selective and stable Mo-doped Co<sub>9</sub>S<sub>8</sub> nanoparticles anchored on Al<sub>2</sub>O<sub>3</sub> matrix by a simple method with CoAl-hydrotalcite as a precursor. According to the characterization results, this multifunctional assembly Mo-Co<sub>9</sub>S<sub>8</sub>/Al<sub>2</sub>O<sub>3</sub> catalyst exhibits electron transfer from Co to Mo sites in Mo-Co<sub>9</sub>S<sub>8</sub> structure, and this Mo-Co<sub>9</sub>S<sub>8</sub> interface has the unique capability for the adsorption of oxygenated compounds. As a consequence, the catalyst exhibits excellent activity in the HDO of diphenyl ether, providing 99.8% conversion and 91.0% yield of benzene under 3 MPa H<sub>2</sub> at 265 °C for 10 h. Moreover, the catalyst displays superior tolerance to high



**Scheme 1.** Illustration on the catalytic mechanism of DPE HDO reaction over the Mo-Co<sub>9</sub>S<sub>8</sub> site.

reaction temperature of 265 °C, and resistance against being poisoned by H<sub>2</sub>O, owing to the anchoring effect of Al<sub>2</sub>O<sub>3</sub> matrix and “protection” of Co<sub>9</sub>S<sub>8</sub>. In particular, it also shows compatibility in the conversion of different substrates including lignin bio-oil and real lignin. This work not only establishes an active and high-temperature stable catalyst (Mo-Co<sub>9</sub>S<sub>8</sub>/Al<sub>2</sub>O<sub>3</sub>) for the HDO of lignin, but also stimulates mechanism understandings and provides an effective strategy to design more efficient and stable sulfide catalysts for high-temperature reactions in the future.

### CRediT authorship contribution statement

Na Ji, Qingling Liu and Changzhi Li co-supervised the whole work. Xingyong Diao and Na Ji conceived the project, designed the experiments and co-wrote the manuscript. Xinxin Li performed the experiments of lignin and lignin oil conversion. Yue Rong performed the kinetics experiments. Yujun Zhao and Xuebin Lu helped to conduct the XPS and TEM measurements. Caixia Liu and Chunfeng Song performed the DFT calculation. Guanyi Chen, Longlong Ma and Shurong Wang gave some sound advice to solve and answer the precious comments provided by the reviewers. Changzhi Li contributed to the X-ray absorption fine structure spectroscopy. All the authors discussed the results and commented on the manuscript.

### Declaration of Competing Interest

The authors declare that they have no known competing financial interests or personal relationships that could have appeared to influence the work reported in this paper.

### Acknowledgements

This work was supported by the National Key R&D Program of China (Grant No. 2018YFB1501500), National Natural Science Foundation of China (22178258, 21975181, 21721004, 21878288), Guangdong Provincial Key Laboratory of New and Renewable Energy Research and Development (No. E139kf0701), and the State Key Laboratory of Pulp and Paper Engineering (South China University of Technology), No. 202113.

### Appendix A. Supporting information

Supplementary data associated with this article can be found in the online version at [doi:10.1016/j.apcatb.2022.121067](https://doi.org/10.1016/j.apcatb.2022.121067).

### References

- C. Li, X. Zhao, A. Wang, G.W. Huber, T. Zhang, Catalytic transformation of lignin for the production of chemicals and fuels, *Chem. Rev.* 115 (2015) 11559–11624.
- N. Ji, X. Diao, Z. Yu, Z. Liu, S. Jiang, X. Lu, C. Song, Q. Liu, D. Ma, C. Liu, Catalytic transfer hydrogenation of ethyl levulinate to  $\gamma$ -valerolactone over supported MoS<sub>2</sub> catalysts, *Catal. Sci. Technol.* 11 (2021) 5062–5076.
- G. Liu, A.W. Robertson, M.M. Li, W.C.H. Kuo, M.T. Darby, M.H. Muhieddine, Y. C. Lin, K. Suenaga, M. Stamatakis, J.H. Warner, S.C.E. Tsang, MoS<sub>2</sub> monolayer catalyst doped with isolated Co atoms for the hydrodeoxygénéation reaction, *Nat. Chem.* 9 (2017) 810–816.
- X. Diao, N. Ji, M. Zheng, Q. Liu, C. Song, Y. Huang, Q. Zhang, A. Alemayehu, L. Zhang, C. Liang, MgFe hydrotalcites-derived layered structure iron molybdenum sulfide catalysts for eugenol hydrodeoxygénéation to produce phenolic chemicals, *J. Energy Chem.* 27 (2018) 600–610.
- N. Ji, X. Diao, X. Li, Z. Jia, Y. Zhao, X. Lu, C. Song, Q. Liu, C. Li, Toward alkylphenols production: lignin depolymerization coupling with methoxy removal over supported MoS<sub>2</sub> catalyst, *Ind. Eng. Chem. Res.* 59 (2020) 17287–17299.
- S.S. Wong, R. Shu, J. Zhang, H. Liu, N. Yan, Downstream processing of lignin derived feedstock into end products, *Chem. Soc. Rev.* 49 (2020) 5510–5560.
- X. Diao, N. Ji, T. Li, Z. Jia, S. Jiang, Z. Wang, C. Song, C. Liu, X. Lu, Q. Liu, Rational design of oligomeric MoO<sub>3</sub> in SnO<sub>2</sub> lattices for selective hydrodeoxygénéation of lignin derivatives into monophenols, *J. Catal.* 401 (2021) 234–251.
- Y. Zhang, T. Liu, Q. Xia, H. Jia, X. Hong, G. Liu, Tailoring of surface acidic sites in Co-MoS<sub>2</sub> catalysts for hydrodeoxygénéation reaction, *J. Phys. Chem. Lett.* 12 (2021) 5668–5674.
- X. Liu, X. Hou, Y. Zhang, H. Yuan, X. Hong, G. Liu, In situ formation of CoMoS interfaces for selective hydrodeoxygénéation of p-cresol to toluene, *Ind. Eng. Chem. Res.* 59 (2020) 15921–15928.
- Z. Luo, Y. Ouyang, H. Zhang, M. Xiao, J. Ge, Z. Jiang, J. Wang, D. Tang, X. Cao, C. Liu, W. Xing, Chemically activating MoS<sub>2</sub> via spontaneous atomic palladium interfacial doping towards efficient hydrogen evolution, *Nat. Commun.* 9 (2018) 2120–2127.
- W. Song, S. Zhou, S. Hu, W. Lai, Y. Lian, J. Wang, W. Yang, M. Wang, P. Wang, X. Jiang, Surface engineering of CoMoS nanosulfide for hydrodeoxygénéation of lignin-derived phenols to arenes, *ACS Catal.* 9 (2019) 259–268.
- S.S. Gronborg, N. Salazar, A. Bruix, J. Rodriguez-Fernandez, S.D. Thomsen, B. Hammer, J.V. Lauritsen, Visualizing hydrogen-induced reshaping and edge activation in MoS<sub>2</sub> and Co-promoted MoS<sub>2</sub> catalyst clusters, *Nat. Commun.* 9 (2018) 2211–2221.
- Y. Huang, Y. Sun, X. Zheng, T. Aoki, B. Pattengale, J. Huang, X. He, W. Bian, S. Younan, N. Williams, J. Hu, J. Ge, N. Pu, X. Yan, X. Pan, L. Zhang, Y. Wei, J. Gu, Atomically engineering activation sites onto metallic 1T-MoS<sub>2</sub> catalysts for enhanced electrochemical hydrogen evolution, *Nat. Commun.* 10 (2019) 982.
- M. Badawi, J.F. Paul, S. Cristol, E. Payen, Y. Romero, F. Richard, S. Brunet, D. Lambert, X. Portier, A. Popov, E. Kondratieva, J.M. Goupil, J. El Fallah, J. P. Gilson, L. Mariey, A. Travert, F. Maugé, Effect of water on the stability of Mo and CoMo hydrodeoxygénéation catalysts: a combined experimental and DFT study, *J. Catal.* 282 (2011) 155–164.
- Y. Zhao, H. Zhou, X. Zhu, Y. Qu, C. Xiong, Z. Xue, Q. Zhang, X. Liu, F. Zhou, X. Mou, W. Wang, M. Chen, Y. Xiong, X. Lin, Y. Lin, W. Chen, H.-J. Wang, Z. Jiang, L. Zheng, T. Yao, J. Dong, S. Wei, W. Huang, L. Gu, J. Luo, Y. Li, Y. Wu, Simultaneous oxidative and reductive reactions in one system by atomic design, *Nat. Catal.* 4 (2021) 134–143.
- Z. Li, X. Lu, W. Sun, L. Leng, M. Zhang, H. Li, L. Bai, D. Yuan, J.H. Horton, Q. Xu, J. Wang, One-step synthesis of single palladium atoms in WO<sub>2.72</sub> with high efficiency in chemoselective hydrodeoxygénéation of vanillin, *Appl. Catal. B* 298 (2021), 120535.
- X. Lu, C. Guo, M. Zhang, L. Leng, J.H. Horton, W. Wu, Z. Li, Rational design of palladium single-atoms and clusters supported on silicoaluminophosphate-31 by a photochemical route for chemoselective hydrodeoxygénéation of vanillin, *Nano Res.* 14 (2021) 4347–4355.
- Z. Li, W. Wei, H. Li, S. Li, L. Leng, M. Zhang, J.H. Horton, D. Wang, W. Sun, C. Guo, W. Wu, J. Wang, Low-temperature synthesis of single Palladium atoms supported on defective hexagonal boron nitride nanosheet for chemoselective hydrogenation of cinnamaldehyde, *ACS Nano* 15 (2021) 10175–10184.
- K. Wu, W. Wang, H. Guo, Y. Yang, Y. Huang, W. Li, C. Li, Engineering Co nanoparticles supported on defect MoS<sub>2-x</sub> for mild deoxygénéation of lignin-derived phenols to arenes, *ACS Energy Lett.* 5 (2020) 1330–1336.
- L. Cattelan, A.K.L. Yuen, M.Y. Lui, A.F. Masters, M. Selva, A. Perosa, T. Maschmeyer, Renewable aromatics from kraft lignin with molybdenum-based catalysts, *ChemCatChem* 9 (2017) 2717–2726.
- A.L. Jongerius, R. Jastrzebski, P.C.A. Bruijninx, B.M. Weckhuysen, CoMo sulfide-catalyzed hydrodeoxygénéation of lignin model compounds: An extended reaction network for the conversion of monomeric and dimeric substrates, *J. Catal.* 285 (2012) 315–323.
- W. Song, W. Lai, Y. Lian, X. Jiang, W. Yang, Sulfated ZrO<sub>2</sub> supported CoMo sulfide catalyst by surface exsolution for enhanced hydrodeoxygénéation of lignin-derived ethers to aromatics, *Fuel* 263 (2020) 116705–116714.
- W. Wang, S. Tan, K. Wu, G. Zhu, Y. Liu, L. Tan, Y. Huang, Y. Yang, Hydrodeoxygénéation of p-cresol as a model compound for bio-oil on MoS<sub>2</sub>: Effects of water and benzo thiophene on the activity and structure of catalyst, *Fuel* 214 (2018) 480–488.
- W. Wang, K. Wu, S. Tan, Y. Yang, Hydrothermal synthesis of carbon-coated CoS<sub>2</sub>-MoS<sub>2</sub> catalysts with enhanced hydrophobicity and hydrodeoxygénéation activity, *ACS Sustain. Chem. Eng.* 5 (2017) 8602–8609.
- K. Wu, C. Wang, X. Chen, W. Wang, Y. Yang, Facile synthesis of hydrophobic MoS<sub>2</sub> and its activity and stability in the hydrodeoxygénéation reaction, *New J. Chem.* 43 (2019) 2734–2739.
- K. Wu, Y. Liu, W. Wang, Y. Huang, W. Li, Q. Shi, Y. Yang, Preparation of hydrophobic MoS<sub>2</sub>, NiS<sub>2</sub>-MoS<sub>2</sub> and CoS<sub>2</sub>-MoS<sub>2</sub> for catalytic hydrodeoxygénéation of lignin-derived phenols, *Mol. Catal.* 477 (2019), 110537.
- H.-B. Wang, J.-Q. Wang, R. Zhang, C.-Q. Cheng, K.-W. Qiu, Y.-j. Yang, J. Mao, H. Liu, M. Du, C.-K. Dong, X.-W. Du, Bionic design of a Mo(IV)-doped FeS<sub>2</sub> catalyst for electroreduction of dinitrogen to ammonia, *ACS Catal.* (2020) 4914–4921.
- H. Zhang, B. Xi, Y. Gu, W. Chen, S. Xiong, Interface engineering and heterometal doping Mo-Ni/Ni(OH)<sub>2</sub> for overall water splitting, *Nano Res.* 14 (2021) 3466–3473.
- M. Ramos, G. Berhault, D.A. Ferrer, B. Torres, R.R. Chianelli, HRTEM and molecular modeling of the MoS<sub>2</sub>-Co<sub>9</sub>S<sub>8</sub> interface: understanding the promotion effect in bulk HDS catalysts, *Catal. Sci. Technol.* 2 (2012) 164–178.
- L. Wang, X. Duan, X. Liu, J. Gu, R. Si, Y. Qiu, Y. Shi, F. Chen, X. Sun, J. Lin, J. Sun, Atomically dispersed Mo supported on metallic Co<sub>9</sub>S<sub>8</sub> nanoflakes as an advanced noble-metal-free bifunctional water splitting catalyst working in universal pH conditions, *Adv. Energy Mater.* 10 (2019) 1903137–1903150.
- L.B. Delmon, Influence of water in the deactivation of a sulfided NiMo- $\gamma$ -Al<sub>2</sub>O<sub>3</sub> catalyst during hydrodeoxygénéation, *J. Catal.* 109 (1994) 281–285.
- E. Laurent, B. Delmon, Study of the hydrodeoxygénéation of carbonyl, carboxylic and guaiacyl groups over sulfided CoMo- $\gamma$ -Al<sub>2</sub>O<sub>3</sub> and NiMo- $\gamma$ -Al<sub>2</sub>O<sub>3</sub> catalysts.1. Catalytic reaction schemes, *Appl. Catal. A* 109 (1994) 77–96.

- [33] V.N. Bui, D. Laurenti, P. Delichère, C. Geantet, Hydrodeoxygenation of guaiacol part II: support effect for CoMoS catalysts on HDO activity and selectivity, *Appl. Catal. B* 101 (2011) 246–255.
- [34] H. Guo, B. Zhang, Z. Qi, C. Li, J. Ji, T. Dai, A. Wang, T. Zhang, Valorization of lignin to simple phenolic compounds over tungsten carbide: impact of lignin structure, *ChemSusChem* 10 (2017) 523–532.
- [35] L. Zhou, M. Shao, C. Zhang, J. Zhao, S. He, D. Rao, M. Wei, D.G. Evans, X. Duan, Hierarchical CoNi-sulfide nanosheet arrays derived from layered double hydroxides toward efficient hydrazine electrooxidation, *Adv. Mater.* 29 (2017) 1604080–1604087.
- [36] J. Liu, S. Xu, W. Bing, F. Wang, C. Li, M. Wei, D.G. Evans, X. Duan, Cu-decorated Ru catalysts supported on layered double hydroxides for selective benzene hydrogenation to cyclohexene, *ChemCatChem* 7 (2015) 846–855.
- [37] S. Wang, K. Zhang, H. Li, L.P. Xiao, G. Song, Selective hydrogenolysis of catechyl lignin into propenylcatechol over an atomically dispersed ruthenium catalyst, *Nat. Commun.* 12 (2021) 416.
- [38] L.L. Feng, G.D. Li, Y. Liu, Y. Wu, H. Chen, Y. Wang, Y.C. Zou, D. Wang, X. Zou, Carbon-armored Co<sub>9</sub>S<sub>8</sub> nanoparticles as all-pH efficient and durable H<sub>2</sub>-evolving electrocatalysts, *ACS Appl. Mater. Interfaces* 7 (2015) 980–988.
- [39] J. Zhang, A. Yang, X. Wu, J. van de Goeij, P. Tang, S. Li, B. Liu, F. Shi, J. Wan, Q. Li, Y. Sun, Z. Lu, X. Zheng, G. Zhou, C.L. Wu, S.C. Zhang, M.L. Brongersma, J. Li, Y. Cui, Reversible and selective ion intercalation through the top surface of few-layer MoS<sub>2</sub>, *Nat. Commun.* 9 (2018) 5289–5298.
- [40] P. Li, Y. Chen, C. Zhang, B. Huang, X. Liu, T. Liu, Z. Jiang, C. Li, Highly selective hydrodesulfurization of gasoline on unsupported Co-Mo sulfide catalysts: effect of MoS<sub>2</sub> morphology, *Appl. Catal. A* 533 (2017) 99–108.
- [41] J.A. Toledo-Antonio, M.A. Cortés-Jácome, C. Angeles-Chávez, J. Escobar, M. C. Barrera, E. López-Salinas, Highly active CoMoS phase on titania nanotubes as new hydrodesulfurization catalysts, *Appl. Catal. B* 90 (2009) 213–223.
- [42] H. Zhu, J. Zhang, R. Yanzhang, M. Du, Q. Wang, G. Gao, J. Wu, G. Wu, M. Zhang, B. Liu, J. Yao, X. Zhang, When cubic cobalt sulfide meets layered molybdenum disulfide: a core-shell system toward synergistic electrocatalytic water splitting, *Adv. Mater.* 27 (2015) 4752–4759.
- [43] M. Kim, M.A.R. Anjum, M. Choi, H.Y. Jeong, S.H. Choi, N. Park, J.S. Lee, Covalent 0D–2D heterostructuring of Co<sub>9</sub>S<sub>8</sub>–MoS<sub>2</sub> for enhanced hydrogen evolution in all pH electrolytes, *Adv. Funct. Mater.* 30 (2020) 2002536–2002546.
- [44] K.-D. Kim, Y.-K. Lee, Promotional effect of Co on unsupported MoS<sub>2</sub> catalysts for slurry phase hydrocracking of vacuum residue: X-ray absorption fine structure studies, *J. Catal.* 380 (2019) 278–288.
- [45] S. Park, J. Park, H. Abroshan, L. Zhang, J.K. Kim, J. Zhang, J. Guo, S. Siahrostami, X. Zheng, Enhancing catalytic activity of MoS<sub>2</sub> basal plane S-vacancy by Co cluster addition, *ACS Energy Lett.* 3 (2018) 2685–2693.
- [46] Y. Kuwahara, N. Furuichi, H. Seki, H. Yamashita, One-pot synthesis of molybdenum oxide nanoparticles encapsulated in hollow silica spheres: an efficient and reusable catalyst for epoxidation of olefins, *J. Mater. Chem. A* 5 (2017) 18518–18526.
- [47] C. Brookes, P.P. Wells, G. Cibin, N. Dimitratos, W. Jones, D.J. Morgan, M. Bowker, Molybdenum oxide on Fe2O3 core–shell catalysts: probing the nature of the structural motifs responsible for methanol oxidation catalysis, *ACS Catal.* 4 (2013) 243–250.
- [48] Y. Okamoto, A. Kato, Usman, N. Rinaldi, T. Fujikawa, H. Koshika, I. Hiromitsu, T. Kubota, Effect of sulfidation temperature on the intrinsic activity of Co-MoS<sub>2</sub> and Co-WS<sub>2</sub> hydrodesulfurization catalysts, *J. Catal.* 265 (2009) 216–228.
- [49] R. Weindl, R. Khare, L. Kovarik, A. Jentys, K. Reuter, H. Shi, J.A. Lercher, Zeolite-stabilized di- and tetranuclear molybdenum sulfide clusters form stable catalytic hydrogenation sites, *Angew. Chem. Int. Ed.* 60 (2021) 9301–9305.
- [50] R. Björnsson, F.A. Lima, T. Spatzal, T. Weyhermüller, P. Glatzel, E. Bill, O. Einsle, F. Neese, S. DeBeer, Identification of a spin-coupled Mo(III) in the nitrogenase iron–molybdenum cofactor, *Chem. Sci.* 5 (2014) 3096–3103.
- [51] X. Wang, R. Rinaldi, A route for lignin and bio-oil conversion: dehydroxylation of phenols into arenes by catalytic tandem reactions, *Angew. Chem. Int. Ed.* 52 (2013) 11499–11503.
- [52] G. Jiang, Y. Hu, G. Xu, X. Mu, H. Liu, Controlled hydrodeoxygenation of phenolic components in pyrolysis bio-oil to arenes, *ACS Sustain. Chem. Eng.* 6 (2018) 5772–5783.
- [53] T. Prasomsri, M. Shetty, K. Murugappan, Y. Román-Leshkov, Insights into the catalytic activity and surface modification of MoO<sub>3</sub> during the hydrodeoxygenation of lignin-derived model compounds into aromatic hydrocarbons under low hydrogen pressures, *Energy Environ. Sci.* 7 (2014) 2660–2669.
- [54] S. Jin, X. Chen, C. Li, C.-W. Tsang, G. Lafaye, C. Liang, Hydrodeoxygenation of lignin-derived diaryl ethers to aromatics and alkanes using nickel on Zr-doped niobium phosphate, *ChemistrySelect* 1 (2016) 4949–4956.
- [55] C. Zhang, J. Lu, X. Zhang, K. MacArthur, M. Heggen, H. Li, F. Wang, Cleavage of the lignin β-O-4 ether bond via a dehydroxylation–hydrogenation strategy over a NiMo sulfide catalyst, *Green Chem.* 18 (2016) 6545–6555.
- [56] D.-Y. Hong, S.J. Miller, P.K. Agrawal, C.W. Jones, Hydrodeoxygenation and coupling of aqueous phenolics over bifunctional zeolite-supported metal catalysts, *Chem. Commun.* 46 (2010) 1038–1040.